Title

On the Parameterization of Convective Downdrafts for Marine Stratocumulus Clouds

Journal

Monthly Weather Review, 148(5)

ISSN

0027-0644

Authors

Wu, Elynn
Yang, Handa
Kleissl, Jan
et al.

Publication Date

2020-05-01

DOI

10.1175/mwr-d-19-0292.1

Peer reviewed

On the Parameterization of Convective Downdrafts to Represent Marine Stratocumulus Clouds

Elynn Wu* , Handa Yang, Jan Kleissl

Center for Renewable Resource and Integration, Department of Mechanical and Aerospace Engineering, University of California, San Diego, La Jolla, CA, USA

Kay Suselj, Marcin J. Kurowski, João Teixeira

Jet Propulsion Laboratory, California Institute of Technology, Pasadena, California

Corresponding author address: Elynn Wu, 9500 Gilman Dr, La Jolla, CA 92093.

E-mail: elw014@eng.ucsd.edu

ABSTRACT

The role of non-local transport on the development and maintenance of marine stratocumulus clouds in coarse resolution models is investigated, with a special emphasis on the downdraft contribution. A new parameterization of cloud-top triggered downdrafts is proposed and validated against large-eddy simulation (LES) for two stratocumulus cases. The applied non-local mass-flux scheme is part of the stochastic multi-plume eddy-diffusivity/mass-flux (EDMF) framework decomposing the turbulence into local and non-local contributions. The local turbulence is represented with the Mellor-Yamada-Nakanishi-Niino (MYNN) scheme. This EDMF version has been implemented in the Weather Research and Forecasting (WRF) single-column model (SCM) and tested for three model versions: without mass flux, with updrafts only, and with both updrafts and downdrafts. In the LES, the downdraft and updraft contributions to the total heat and moisture transport are comparable and significant. The WRF SCM results show a good agreement between the parameterized downdraft turbulent transport and LES. While including updrafts greatly improves the modeling of Sc clouds over simulation without mass flux, the addition of downdrafts better simulates the moisture profile in the planetary boundary layer.

1. Introduction

Stratocumulus (Sc) clouds are one of the most common cloud types on Earth (Hahn and Warren 2007). They form under strong temperature inversions and are prevalent off the western coast of continents, on the descending side of the Hadley cell. Their impact on the Earth's energy budget is significant as they strongly reflect incoming solar radiation, with a much weaker effect on outgoing longwave radiation (Wood 2012). Accurate modeling of Sc clouds has high importance for several reasons: (i) they are one of the key sources of uncertainty in climate predictions (Bony and Dufresne 2005; Zelinka et al. 2017), (ii) they affect solar power integration into the electric grid (Yang and Kleissl 2016; Zhong et al. 2017; Wu et al. 2018), and (iii) they impact aviation by hindering the takeoff and landing of flights (Reynolds et al. 2012).

Physical processes governing the evolution of the stratocumulus-topped boundary layer (STBL)— such as cloud-top radiative cooling, entrainment, evaporative cooling, surface fluxes, wind shear, and precipitation— widely range on spatial and temporal scales, and modeling Sc clouds is quite challenging as a result (e.g. Lilly 1968; Stevens 2002; Wood 2012). Efforts through both observational campaigns (e.g. Stevens et al. 2003; Malinowski et al. 2013; Crosbie et al. 2016) and high resolution numerical modeling (e.g. Stevens et al. 2005; Kurowski et al. 2009; Yamaguchi and Randall 2011; Chung et al. 2012; Blossey et al. 2013; de Lozar and Mellado 2015; Pedersen et al. 2016; Mellado et al. 2018; Matheou and Teixeira 2019) have significantly advanced our understanding of the physics of Sc clouds. These physical insights are important for numerical weather prediction (NWP) and general circulation models (GCMs) where grid resolution is coarse.

The picture emerging from those studies is that cloud-top radiative cooling is a critical source of STBL turbulence (Matheou and Teixeira 2019), contributing to cloud-top entrainment (Mellado 2017). The combined effect of both evaporative and radiative cooling— the former typically

enhanced by wind shear (Mellado et al. 2014)— destabilizes the top of cloud layer through buoyancy reversal that leads to the formation of negatively buoyant weak downdrafts. This process is often considered responsible for the generation of cloud holes in largely unbroken Sc clouds (Gerber et al. 2005; Kurowski et al. 2009). Many small-scale phenomena (e.g., entrainment, shear, evaporative cooling, cloud microphysics) are at play in the origin of downdrafts and can strongly influence vertical mixing (Mellado 2017). Exactly how these processes interact with each other remains a research challenge.

Turbulent transport in the STBL is the main driver to the formation, maintenance, and dissipation of Sc clouds. In coarse-resolution models, turbulent transport is typically parameterized using simplified one-dimensional planetary boundary layer (PBL) schemes. Global NWP models (e.g. Teixeira 1999) and climate models tend to underestimate Sc clouds (Teixeira et al. 2011; Lin et al. 2014), although there is an improvement in the representation of the radiative properties by a newer generation of climate models (Engström et al. 2014). In terms of mesoscale models, Ghonima et al. (2017) compared three different PBL schemes in the Weather Research and Forecasting (WRF) model and found that they all underestimate entrainment, producing too moist and cold STBLs. Huang et al. (2013) compared five different WRF PBL parameterizations and highlighted the difficulties of simulating the STBL. Recent studies supported the importance of downdrafts in transporting turbulent heat and moisture flux in the PBL (Chinita et al. 2017; Davini et al. 2017; Brient et al. 2019) through analyzing LES of STBL. Brient et al. (2019) concluded that for a more accurate parameterization of turbulence within STBL, downdrafts should be explicitly included in climate models. Downdrafts were recently implemented by Han and Bretherton (2019) in a turbulent kinetic energy (TKE)-based moist Eddy-Diffusivity/Mass-Flux (EDMF) parameterization within the GFS model, and they found more accurate liquid water and wind speed profiles for marine STBLs.

This study introduces parameterized downdrafts into NWP and aims at investigating their impact on the evolution of the STBL. To test whether convective downdrafts are necessary to properly represent Sc clouds, we implement a new downdraft parameterization in WRF based on the EDMF approach that uses Mellor-Yamada-Nakanishi-Niino (MYNN) as the ED component. This differs from Han and Bretherton (2019) where different ED and MF models were used and additional features were implemented to advance the vertical turbulence mixing parameterization for not only STBL but also other conditions. We place a special emphasis on evaluating the role of non-local transport in STBL with gradual changes to the model in order to separate effects coming from convective downdrafts. The new parameterization is evaluated in two typical STBL cases.

Section 2 describes the EDMF and MYNN schemes as well as the updraft and downdraft implementation in WRF. The numerical design of the LES setup, WRF single column model (SCM), and updraft and downdraft properties are described in Section 3. WRF SCM results for both STBL cases are shown in Section 4. Finally, conclusions are presented in Section 5.

2. PBL scheme with downdrafts

In coarse resolution atmospheric models, the PBL scheme determines turbulent flux profiles within the PBL as well as the overlying air, providing tendencies of temperature, moisture, and horizontal momentum due to mixing and turbulent transport for the entire atmospheric column. This section first gives an overview of the EDMF framework, then the details of ED and MF models are presented (Sections 2b and 2c). The properties of updrafts and downdrafts are diagnosed using LES and presented in Section 3 in order to quantify the validity of the parameterized mass-flux model.

a. The Eddy-Diffusivity/Mass-Flux (EDMF) Approach

Siebesma and Teixeira (2000); Teixeira and Siebesma (2000); Siebesma et al. (2007) introduced the eddy diffusivity/mass-flux (EDMF) approach for parameterizing turbulence in a dry convective boundary layer, and additional improvements have been made by Witek et al. (2011). The idea behind EDMF is to parameterize the turbulent fluxes as a sum of local transport through ED and non-local transport through a mass-flux contribution. The EDMF approach has been extended to represent moist convection since then (e.g. Soares et al. 2004; Neggers et al. 2009; Neggers 2009; Angevine et al. 2010, 2018; Suselj et al. 2013, 2019a,b). In these papers, the updrafts start out as dry and begin to condense when the conditions are right. In other words, moist updrafts are a result of dry updrafts. The EDMF approach provides an unified parameterization of boundary layer and moist convection, and it is thus an ideal framework for modeling STBL.

b. ED scheme: The Mellor-Yamada Nakanishi and Niino (MYNN)

The ED component we use is the level 2.5 Mellor-Yamada Nakanishi and Niino (MYNN) model, which is a modified Mellor-Yamada turbulence closure scheme originally developed by Mellor and Yamada (1982), with significant improvements made over the years (Nakanishi and Niino 2006, 2009). In MYNN, vertical turbulent fluxes are modeled according to K-theory:

$$\overline{w'\varphi'} = -K\frac{\partial \varphi}{\partial z}, \tag{1}$$

where eddy diffusivity K is parameterized as a function of the TKE (q), master length scale L, and stability correction functions $S_{h,m}$, which differ for heat and momentum:

$$K_{h,m}(z) = q(z)L(z)S_{h,m}(z). \tag{2}$$

The prognostic thermodynamic equations in MYNN use moist conserved variables: liquid water potential temperature θ_l and total water mixing ratio q_t. The prognostic dynamic variables are the

horizontal components of wind u and v. An additional prognostic equation of the MYNN Level 2.5 model solves the (doubled) subgrid TKE: $q^2 = 2 \times TKE = \overline{u'^2} + \overline{v'^2} + \overline{w'^2}$, and is formulated as:

$$\frac{\partial q^2}{\partial t} = -\frac{\partial}{\partial z}\left(LqS_q \frac{\partial q^2}{\partial z}\right) - 2\left(\overline{u'w'}\frac{\partial U}{\partial z} + \overline{v'w'}\frac{\partial V}{\partial z}\right) + 2\frac{g}{\theta_0}\overline{w'\theta'_v} - 2\varepsilon. \quad (3)$$

Eq. 3 describes the tendency of TKE, due to turbulent and pressure transport, shear production, buoyant production, and turbulent dissipation. L is the master length scale as in Eq. 2, and $S_q = 3S_m$ is the stability correction function for TKE (see Nakanishi and Niino (2009) for detailed formulations). L is designed such that the smallest length scale out of three different formulations dominates at a given level. The first formulation is the surface length scale L_{sfc}, which is the Prandtl mixing length corrected for stability. It is small near the surface, but increases rapidly with height. The second one, the turbulent length scale for a well-mixed layer L_{turb}, is formulated as a function of the vertically-integrated TKE, independent of height. Finally, the buoyancy length scale L_{buoy} is computed as a function of local stratification (i.e., $\frac{\partial \theta_v}{\partial z}$), and it decreases with increasing stratification. The buoyancy length scale is only active in stable conditions. The stability functions for heat and moisture $S_{h,m}$ contain empirical constants, which generally decrease with increasing stability, as they are inversely related to the Richardson number (Eq. 27 and 28 in Nakanishi and Niino 2009). Finally, the dissipation rate is parameterized as $\varepsilon = \frac{q^3}{B_1 L}$, where B_1 is a closure constant (B_1 = 24 in the MYNN scheme).

c. Adding mass flux to MYNN

The MYNN Level 2.5 ED model determines turbulent mixing at each vertical level based on the gradients in scalars between immediately adjacent vertical levels (Eq. 1). When deep mixing due to larger eddies becomes important, the MYNN scheme has been shown to produce erroneous thermodynamic profiles (Huang et al. 2013). Non-local models, such as the YSU and ACM2 schemes,

account for this deep mixing by using a counter-gradient term (Hong et al. 2006) or a transilient mass flux matrix (Pleim 2007). Another common approach is the EDMF framework, which decomposes the subgrid vertical mixing into local mixing through ED and non-local (mass-flux; MF) transport through convective plumes. Traditionally, PBL schemes, such as MYNN, model the turbulence within the PBL through only ED. In the EDMF framework, ED is used to model the non-convective transport in the non-convective environment, with an additional contribution from the MF portion.

1) MASS FLUX MODEL OVERVIEW

To represent non-local transport, we use the stochastic multi-plume EDMF model. The idea behind this model is that the horizontal subgrid domain is composed of an ensemble of convective plumes and the remaining non-convective environment. The multi-plume approach is designed to account for the non-linear interactions between the plumes and the environment, as the entrainment with the environment is stochastic for each plume. Following the same notation as Suselj et al. (2019a,b), the grid-mean value of any variable φ can be written as:

$$\overline{\varphi} = \sum_{n=1}^{N} a_{u_n}\varphi_{u_n} + \sum_{m=1}^{M} a_{d_m}\varphi_{d_m} + a_e\varphi_e, \tag{4}$$

where N/M is the total number of updrafts/downdrafts. The subscripts u_n, d_m, and e denote mean values from the $n-th$ updraft, $m-th$ downdraft, and the environment, while a_{u_n}, a_{d_m}, and a_e are the corresponding areas. In WRF, assuming the fractional area of updraft and downdraft are small, we approximate $\overline{\varphi} \approx \varphi_e$, and the turbulent flux can be written as (see Eqs. 7 in Suselj et al. (2019b)):

$$\overline{w'\varphi'} = \sum_{n=1}^{N} a_{u_n}(\varphi_{u_n} - \overline{\varphi})(w_{u_n} - \overline{w}) + \sum_{m=1}^{M} a_{d_m}(\varphi_{d_m} - \overline{\varphi})(w_{d_m} - \overline{w}) + a_e\overline{w'\varphi'}|_e, \tag{5}$$

where the vertical transport of non-convective environment $\overline{w'\varphi'}|_e$ is modeled using Equation 1.

2) SURFACE-DRIVEN UPDRAFTS

A version of EDMF including surface-driven updrafts (Olson et al. 2019) has been implemented as an add-on option in MYNN since WRF v3.8 and is used for NOAA's operational Rapid Refresh (RAP; Benjamin et al. (2016)) and High Resolution Rapid Refresh (HRRR) forecast systems. The original version of this dynamic multi-plume mass-flux scheme in WRF v3.8 ($bl\_mynn\_edmf = 1$) followed Suselj et al. (2013), but the version in the current WRF v4.0 contains considerable changes from the original form. We do not base our EDMF implementation ($bl\_mynn\_edmf = 3$) on what is currently available in WRF, but instead follow Suselj et al. (2013) and Suselj et al. (2019a,b). The numerical implementation is documented in Suselj et al. (2019b) (Appendix B).

The surface-driven updrafts are represented by an ensemble of steady-state plumes with different initial conditions and stochastic entrainment rates. The thermodynamic and dynamic properties of the n-th updraft $\varphi_{u_n} = \{\theta_{l,u_n}, q_{t,u_n}, u_{u_n}, v_{u_n}\}$ follow:

$$\frac{\partial \varphi_{u_n}}{\partial z} = \varepsilon_{u_n}(\overline{\varphi} - \varphi_{u_n}), \tag{6}$$

where ε_{u_n} is the entrainment rate. Note that an additional source term, due to microphysical processes in Suselj et al. (2019b), is not included here as it has no effect in non-precipitating STBL. The number of updrafts is fixed to ten ($n = 1, ..., N$; $N = 10$). The steady-state equation of the updraft velocity is:

$$\frac{1}{2}\frac{\partial w_{u_n}^2}{\partial z} = a_w B_{u_n} - (b_w \varepsilon_{u_n} + P_{w_{ud}}) w_{u_n}^2, \tag{7}$$

where $a_w = 1$, $b_w = 1.5$ are model constants (de Roode et al. 2012; Suselj et al. 2013, 2019b). Variable $B_{u_n} = g(\theta_{v,u_n}/\overline{\theta}_v - 1)$ is the updraft buoyancy, and $\theta_v = \theta(1 + 0.61 q_v - q_l)$ is the virtual potential temperature. $P_{w_{ud}}$ represents the dynamical pressure effects as updrafts approach the

inversion and is parameterized as:

$$p_{w_{ud}} = \begin{cases} \frac{1-exp((z_i-z)/z_{00}-1)}{0.1(z_i-z)}, & z > (z_i - z_{00}) \\ 0, & z \leq (z_i - z_{00}), \end{cases} \tag{8}$$

where z_{00} denotes the distance from z_i when $p_{w_{ud}}$ starts to be in effect. For this work, we use $z_{00} =$ 100 m. Assuming a normal distribution of the vertical velocity near the surface, the updrafts are thought to represent the positive tail of the distribution, between one and three standard deviations, divided into N bins. This results in a total updraft area of approximately 15% near the surface. The thermodynamic surface conditions for the updrafts are identical to Suselj et al. (2019a) (Appendix A). ε_{u_n} is the stochastic entrainment rate, computed as:

$$\varepsilon(\Delta z) = \frac{\varepsilon_0}{\Delta z} P\left(\frac{\Delta z}{L_\varepsilon}\right), \tag{9}$$

$$L_\varepsilon = L_0 exp(-c_{ent} z/z_i), \tag{10}$$

where $\varepsilon_0 = 0.2$ is the fractional mass of air entrained in a single entrainment event. $P(\lambda)$ is a random number drawn from the Poisson distribution with parameter $\lambda = \left(\frac{\Delta z}{L_\varepsilon}\right)$, which represents the number of entrainment events a single updraft experiences over height Δz. $L_0 = 100$ m denotes the distance a plume needs to travel to entrain once. The exponential term in Eqs. 10 represents the dynamic effect near strong temperature inversion, as the updrafts cannot penetrate above that layer and are assumed to entrain more and disintegrate, where $c_{ent} = 0.5$ is a model constant controlling how fast entrainment length decreases with height. For STBL, we use the cloud-top height z_i (also known as the inversion height) to denote where this dynamic effect is at its strongest. z_i is defined as the last point near the PBL height where $q_l > 10^{-6}$ kg kg^{-1}, and cloud fraction is greater than 50%. This definition of locating z_i is identical to that in Olson et al. (2019), where they included an option for top-down buoyancy production in ED when Sc clouds were present. In the MYNN parameterization, there are three options to represent sub-grid cloudiness, which are controlled by

197 $bl\_mynn\_cloudpdf$ parameter. In this work, $bl\_mynn\_cloudpdf = 1$, for which a statistical partial
198 condensation cloud scheme based on joint-Gaussian probability distribution function of θ_l and q_t
199 is used (Kuwano-Yoshida et al. 2010). By default, the Gaussian PDFs are applied to the whole
200 grid box (i.e., including non-convective environment and convective updrafts and downdrafts).
201 We thus assume that Gaussian distributions of the thermodynamic variables (cf. Figure 1) yield
202 reasonably accurate cloud cover and liquid water values for STBL. Cloud fraction would ideally
203 be computed from Eqs. 4, and we use this approximation for simplicity. Note that for STBL,
204 saturation conditions are usually met for most of the PDFs area.

205 While Suselj et al. (2013) did not include either the dynamical pressure effect (i.e. $P_{w_{ud}}$ term
206 in Eqs. 7) or modification of entrainment length (L_ε) by proximity of inversion for the STBL
207 simulation, we find that those modifications yield results that are more consistent with the plume
208 statistics in LES, as discussed further in Section 3. The entrainment rate is the same for all vari-
209 ables (θ_{l,u_n}, q_{t,u_n}, u_{u_n} and v_{u_n}). Although Suselj et al. (2019b) used $\frac{1}{3}\varepsilon_{u_n}$ for u_{u_n} and v_{u_n}, we find
210 that equal entrainment rate results in better u and v profile.

211 Since each updraft is characterized by different surface conditions and entrainment rates, the
212 thermodynamic properties and termination heights also differ. Each plume is integrated indepen-
213 dently in the vertical until the vertical velocity becomes negative. Condensation occurs within a
214 plume if its total water mixing ratio exceeds the saturated water mixing ratio. Therefore, there exist
215 dry and partly moist plumes among the N updrafts, and the fate of each plume is determined by its
216 initial conditions, dynamical pressure effect, and lateral entrainment with the environment. Since
217 each individual updraft is integrated independently, whenever vertical velocity becomes negative
218 and terminates, the updraft area is reduced. This can often be seen in regions with strong lateral
219 entrainment rates.

3) CLOUD-TOP TRIGGERED DOWNDRAFTS

Several important physical processes are at play near the STBL top. Radiative and evaporative cooling produces cooled downdrafts and drives buoyant production of turbulence in the PBL. Entrainment from the free troposphere can impact downdrafts near the cloud-top: warm air from the free troposphere counteracts the radiative cooling and buoyant production of turbulence. When the PBL is less turbulent, the entrainment rate decreases, indicating a negative feedback loop (Wood 2012). Surface-driven updrafts may also affect the downdrafts. As updrafts approach the inversion, they begin to diverge and can help initiate or enhance downdrafts (Kurowski et al. 2009; Davini et al. 2017). This enhances the downdraft vertical velocity and, in turn, the turbulence in the PBL. In the proposed parameterization of downdrafts, those dependencies are important for the formulation of the downdraft initial conditions. Our downdraft parameterization in MYNN can be activated by specifying $bl\_mynn\_edmf\_dd = 1$ in the namelist. The numerical implementation follows Suselj et al. (2019b) (Appendix C).

Similar to the surface-driven updrafts, downdrafts are also represented by an ensemble of steady-state plumes with stochastic lateral entrainment. The thermodynamic and dynamic properties of the m-th downdraft $\varphi_{d_m} = \{\theta_{l,d_m}, q_{t,d_m}, u_{d_m}, v_{d_m}\}$ follow:

$$\frac{\partial \varphi_{d_m}}{\partial z} = -\varepsilon_{d_m}(\overline{\varphi} - \varphi_{d_m}). \tag{11}$$

$\varepsilon_{d_m} = \frac{\varepsilon_0}{\Delta z} P\left(\frac{\Delta z}{L_\varepsilon}\right)$ is the entrainment rate similar to Equation 9, where $L_\varepsilon = L_0$, and the values of L_0 and ε_0 are the same as for the updrafts. The entrainment rate is same for $\theta_{l,dm}$ and $q_{t,dm}$, however, it is increased to 1.4 times for u_{dm} and v_{dm}. We find that increasing entrainment rate for momentum results in better u and v profile. The additional source term due to microphysical processes in Suselj et al. (2019b) is neglected here. The number of downdrafts is fixed to ten ($m = 1, ..., M$; $M = 10$). The steady-state equation of the downdraft velocity is identical to Suselj et al. (2019b) :

$$\frac{1}{2}\frac{\partial w_{d_m}^2}{\partial z} = a_w B_{d_m} + (b_w \varepsilon_{d_m} + p_{w_{dd}}) w_{d_m}^2, \tag{12}$$

where $p_{w_{dd}}$ represents the dynamical pressure effects as downdrafts approach the surface and is parameterized as:

$$p_{w_{dd}} = \begin{cases} \frac{1-exp(z/z_{00}-1)}{2z}, & z \leq z_{00} \\ 0, & z > z_{00}, \end{cases} \tag{13}$$

where $z_{00} = 100$ m. This is equivalent to the dynamical pressure effect in updraft, except we replace z_i with 0.

We assume downdrafts start randomly in the upper half of the cloud layer.. We avoid starting all downdrafts at z_i to avoid numerical instabilities in this region during model spin-up time. The reason behind this choice is described in more details in next section. Similarly to the updraft parameterization, we assume that the downdrafts represent the negative tail of the vertical velocity distribution which is assumed to be normal (between negative one and three standard deviations), resulting in a total downdraft area of approximately 15% slightly below cloud-top. The formulation of cloud-top conditions for downdrafts is similar to the formulation for surface-driven updrafts (Suselj et al. 2019a). The difference lies in the parameterization of the variances of vertical velocity σ_w, total water mixing ratio σ_{q_t}, and virtual potential temperature σ_{θ_v}. The strength of downdraft vertical velocity is proportional to σ_w:

$$\sigma_w = c_1 w_{*,dd}, \tag{14}$$

where $c_1 = 0.3$ is a model constant. $w_{*,dd}$ is the the convective vertical velocity scale which takes into account both the intensity of surface-driven updrafts and cloud-top radiative cooling and is similar to the entrainment parametrization in Ghonima et al. (2017):

$$w_{*,dd} = \left[0.15(w_*^3 + 5u_*^3) + 0.35 w_{rad}^3\right]^{1/3}, \tag{15}$$

where $w_* \equiv (g/\theta_v)\overline{w'\theta'_v}|_s z_{top}$ is the Deardorff convective velocity scale, u_* is the surface friction velocity, and $w_{rad} \equiv (g/\theta_v)\overline{w'\theta'_v}|_{rad} z_{top}$ is a velocity scale based on the net radiative flux divergence at the cloud-top where $\overline{w'\theta'_v}|_{rad} = \frac{F_{rad}}{\rho c_p}$ (Lock and Macvean 1999). In WRF, F_{rad} is defined as the radiative flux divergence between cloud-top and cloud base.

The framework of parameterizing σ_{q_t} and σ_{θ_v} is similar to that described by Köhler (2006). The downdraft initial total mixing ratio deficit is proportional to σ_{q_t}:

$$\sigma_{q_t} = c_2 q_*, \tag{16}$$

where $c_2 = 30$ is a model constant, and $q_* \equiv \frac{\overline{w'q'_t}_{ent}}{w_{rad}}$ is the moisture scale due to mixing with entrained air. The entrainment fluxes $\overline{w'\varphi'}_{ent}$ are modeled according to the flux-jump relation $\overline{w'\varphi'}_{ent} = w_e \Delta\varphi_{z_{inv}}$ (Lilly 1968), where $\Delta\varphi_{z_{inv}} = \varphi_{z_{inv+1}} - \varphi_{z_{inv}}$ represents the jump value of the scalar φ across the inversion. w_e is the entrainment velocity and is parameterized following Ghonima et al. (2017):

$$w_e = -\frac{\theta_{v0}}{g\Delta\theta_{v,inv} z_{inv}}\left[0.15(w_*^3 + 5u_*^3) + 0.35 w_{rad}^3\right]. \tag{17}$$

In WRF, the jump in moisture, Δq_t, is defined as the difference in q_t at 700 hPa and the surface.

The downdraft initial virtual potential temperature is proportional to σ_{θ_v}:

$$\sigma_{\theta_v} = c_3 \theta_{v,*}, \tag{18}$$

where $c_3 = 1$ is a model constant, and $\theta_{v,*} \equiv \frac{\overline{w'\theta'_v}_{ent}}{w_{*,rad}}$ is the buoyancy scale due to mixing with entrained air and radiative cooling. The jump in heat, $\Delta\theta_v$, is similar to (Wood and Bretherton 2006):

$$\Delta\theta_v = (\theta_{v,700} - \theta_{v,0}) - \Gamma_{FT}(z_{700} - z_{inv}), \tag{19}$$

where $\theta_{v,700}$ is θ_v at p = 700 hPa, $\theta_{v,0}$ is θ_v at the surface, Γ_{FT} is the free tropospheric adiabat, and z_{700} is the height of the $p = 700$ hPa surface. Since difference in θ_v at 700 hPa and the surface

is a combination of temperature increase across the capping inversion and the accumulated static stability between this inversion and the 700 hPa reference level, we subtract $\Gamma_{FT}(z_{700} - z_{inv})$ to focus on temperature jump across the inversion. We find this definition of inversion jumps to be more systematic and consistent than attempting to diagnose the exact point where the temperature inversion begins and ends.

Similar to the updrafts, equations for each downdraft are integrated independently in the vertical until the vertical velocity becomes positive. Condensation occurs within a downdraft if its total water mixing ratio exceeds the saturated water mixing ratio. Similarly to updrafts, there exist dry and partly moist plumes among the M downdrafts, and the fate of each plume is determined by its initial conditions, dynamical pressure effect, and lateral entrainment with the environment. Since each individual downdraft is integrated independently, whenever vertical velocity becomes positive and terminates, the downdraft area is reduced. This is often the case in regions with strong lateral entrainment rates.

3. Design of Numerical Experiments

a. LES Setup

Large eddy simulations are performed using the UCLA-LES model (Stevens 2010) and treated as "ground truth." Two idealized non-drizzling marine Sc cases are chosen as baseline simulations: the DYCOMS-II RF01 (Stevens et al. 2005) and CGILS S12 Control (Blossey et al. 2013) (hereinafter DYCOMS and CGILS). The experiments are set up following the respective intercomparison studies. Interactive radiation is treated differently in the two cases. Specifically, a simplified model of radiative forcing matching the δ-four stream transfer code (Stevens et al. 2005) is used in DYCOMS. As for CGILS, a full radiative transfer code is used, which utilizes Monte Carlo

sampling of the spectral integration (Pincus and Stevens 2009). The DYCOMS case is run for 4 h, and the CGILS case is run for 24 h. While we focus our analysis of the updraft and downdraft properties on nocturnal quasi-steady conditions (first 4 h), the 24 h simulation of CGILS provides reference to the generalization of the parameterization during the day. In both experiments, a non-uniform vertically-stretched grid is used with 5 m resolution around the inversion, and a several times coarser resolution in the horizontal. This LES setup is identical to that in Ghonima et al. (2017). A summary of the model setups is provided in Table 1.

1) Determining plume properties

Simulation outputs are stored at one minute intervals from hour three to four in order to gather updraft and downdraft properties. The statistics are averaged over one hour. We use the joint normal probability density function (PDF) between vertical velocity w, total water mixing ratio ($q_t = q_v + q_l$), virtual potential temperature ($\theta_v = \theta(1 + 0.61q_v - q_l)$), and liquid water potential temperature ($\theta_l = \theta - (L_v q_l)(c_p \pi)^{-1}$) to define LES updrafts and downdrafts. L_v is the latent heat of vaporization, c_{pd} is the specific heat of dry air at constant pressure, π is the Exner function, and subscripts are v for vapor, l for liquid. We define the normalized variable to be $\varphi' = \frac{\varphi - \overline{\varphi}}{\sigma_\varphi}$, where $\overline{\varphi}$ is the slab mean and σ_φ is the standard deviation of φ. By carefully investigating the joint PDFs, we define updrafts to be the LES grid-points that conform to the following conditions: $w' > 1$, $q_t' > 0$, and either $\theta_l' < 0$ or $\theta_v' > 0$. We define downdrafts to be $w' < 0$, $q_t' < -1$, and $\theta_l' > 0$. Specifically, this definition of downdrafts captures the negative tail in the joint normal PDF. Figure 1 shows the joint normal PDF for DYCOMS at a normalized height close to the cloud-top ($z/z_i = 0.97$). A strong negative tail is observed in Figure1A, where $w' < 0$ and $q_t' < -1$. We also confirm that grid-points satisfying these criteria correspond well with negatively buoyant ($\theta_v' < 0$) parcels that are warmer in terms of the liquid water potential temperature ($\theta_l' > 0$). While

the definitions of updraft and downdraft used here are not as rigorous as in Chinita et al. (2017); Davini et al. (2017); Brient et al. (2019), we find that the overall properties are consistent with their study.

The mean downdraft and updraft properties are shown in Figure 2 for DYCOMS and Figure 3 for CGILS. Updraft and downdraft areas are comparable in the middle of the PBL (Figure 2A & 3A), with updrafts decreasing near cloud-top and downdrafts decreasing before reaching the surface. Figure 2B & C and Figure 3B & C show partial contributions to the total heat and moisture fluxes from the environment, updrafts, and downdrafts. Similar results are found in both STBL cases: cloud-top entrainment heat flux is largely from updrafts; the peak in downdraft heat and moisture transport is slightly below the peak in updrafts ($\approx$100 m lower); heat and moisture transport from downdrafts is stronger than updrafts in cloudy region; environmental mean of w, θ_l, θ_v, q_t, and q_l is very close to the grid mean. Both cases have similar updraft and downdraft properties: downdrafts terminate before reaching the surface (Figure 2A & Figure 3A); updraft and downdraft vertical velocity are approximately a mirror image of each other (Figure 2D & Figure 3D); downdrafts become negatively buoyant ($\theta_v' < 0$) slightly below cloud-top (Figure 2F & Figure 3F); updrafts correspond to thicker cloud regions and downdrafts are co-located with cloud holes (Figure 2H & Figure 3H). Since the peak in downdraft heat and moisture transport is slightly below the peak in updraft, the choice of starting downdrafts randomly between cloud-top and half way through cloud-base is consistent with the findings in LES.

The properties shown in these two STBL cases compare well to the case in Brient et al. (2019), where the First ISCCP Regional Experiment (FIRE) study was simulated for 24 h to study the diurnal cycle of coherent updraft and downdraft properties. Specifically, the nighttime results of Brient et al. (2019) show that the areas of updrafts and downdrafts are comparable in the middle of the PBL (around 12%) and the downdraft area decreases quickly to zero below 100 m, which cor-

responds well with our findings for DYCOMS. CGILS results show a slightly smaller downdraft area in the middle of the PBL (around 9%). The turbulent heat flux in Brient et al. (2019) shows that the transport of heat by updrafts is the strongest at cloud-top, the peak of the downdraft heat transport is slightly below that for the updrafts (≈50 m lower), and the heat transport by updrafts in cloudy region is nearly zero when downdrafts dominate. This corresponds well with DYCOMS, while updrafts in CGILS have a slightly positive heat transport in the cloudy region. As for the turbulent moisture flux, Brient et al. (2019) shows that updrafts dominate from the surface up to slightly above cloud base, while downdrafts dominate in the cloud layer. Moisture flux is similar in DYCOMS and CGILS, but our results show a positive peak of updraft moisture flux near cloud-top, making the updraft contribution to the moisture flux a dominating term around cloud-top. Chinita et al. (2017) shows large differences in the contribution of updrafts and downdrafts to total flux for DYCOMS in the cloud layer. In general, they find that updrafts account for most of the organized motions near the surface, while downdrafts are more important near the boundary layer top. While the overall properties are similar, updraft and downdraft areas in Chinita et al. (2017) are 5 to 10 % larger.

b. WRF single column model

DYCOMS and CGILS case are simulated using the Weather Research and Forecasting (WRF) v4.0 single column model (SCM) and compared against LES. Initial conditions and forcing are identical to that in LES (i.e., fixed surface fluxes for DYCOMS and CGILS, large-scale subsidence as in Table 1) and was used previously in Ghonima et al. (2017). The SCM vertical domain includes 116 levels to resolve the lowest 12 km of the troposphere, which comes out to be $\Delta z \approx 20$ m in the first 1 km. A simulation time step of 40 s is used. In Section 4c, we show that results are insensitive when the time step is decreased. Three different versions of one PBL scheme

are used to determine the importance of the introduced changes: 1) the original Mellor-Yamada-Nakanishi-Niino scheme (MYNN; hereinafter ED) (Nakanishi and Niino 2006, 2009), 2) MYNN with updrafts (EDMF$_U$), and 3) MYNN with updrafts and downdrafts (EDMF$_{UD}$). For EDMF$_U$ and EDMF$_{UD}$, the MYNN scheme is used as a parameterization of local transport in the non-convective environment. The radiation scheme is RRTMG (Iacono et al. 2008). No microphysics or cumulus schemes are used since both cases represent non-precipitating STBL.

4. Results

a. DYCOMS-II RF01

Figure 4 shows the mean fields of θ_l, q_t, q_l, u, n, heat flux ($\rho c_p \overline{w'\theta_l'}$), and moisture flux ($\rho L_v \overline{w'q_t'}$). Figure 5 shows the time series of liquid water path (LWP), boundary layer averaged heat (θ_l), and moisture (q_t) for the three tested PBL schemes and LES. ED has a cold and moist bias in the PBL (Figure 5B and C), resulting in an overestimation of LWP for the entire simulation. The underestimation of entrainment flux is likely the cause of this behavior as ED fails to model heat and moisture transport between the free-troposphere and the PBL (Figure 4G & H). Moreover, ED does not have a transition in horizontal wind between the PBL and the free troposphere, indicating that ED does not capture the momentum transport properly (Figure 4E & F). EDMF$_U$ has a weaker cold and moist bias, and the bias in LWP is minimal during hour 3 to 4. However, inversion base height is slightly lower than ED. This is a result of updrafts overshooting into the free troposphere in the early time of the simulation, mixing out the initial inversion base height. EDMF$_{UD}$ has a much smaller bias in boundary layer averaged heat and moisture and has a more well-mixed profile in q_t than EDMF$_U$. Inversion base height is also slightly lower in EDMF$_{UD}$. Both EDMF$_U$ and EDMF$_{UD}$ capture the entrainment heat and moisture flux well. Among the three

tested PBL schemes, EDMF$_U$ has the best match in horizontal wind in the PBL, and EDMF$_{UD}$ overestimates u but underestimates v in the PBL.

Figures 6 and 7 show the vertical flux contribution from the individual components: environment (ED), updraft, and downdraft. Figure 6 is for EDMF$_U$, which includes only ED and updraft. Note that LES transport in 6A & D includes LES environmental and downdraft transport because in the case of updrafts only, the remaining area is considered to be the environment and should therefore be modeled by ED. Updraft contribution to the heat flux matches the profile in LES well, however it is overestimated in most of PBL and the cloud-top entrainment heat flux is too strong. It is important to note that cloud-top entrainment is not fully understood even in LES. We find here that even though entrainment heat flux appears to be strong, boundary layer averaged temperature in EDMF$_U$ is still too cold compared to LES (Figure 5B). However, EDMF$_U$ produces a warmer boundary layer compared to ED, which strongly underestimates entrainment heat flux. Updraft contribution to the moisture flux is overestimated throughout the PBL, but ED component is underestimated and the total moisture flux matches LES well. The initial updraft starting θ_l and q_t are stronger than LES (not shown) and eventually leads to overestimation of moisture flux. This indicates that the formulation of updraft surface condition in STBL may be different from shallow convection since we retain the same updraft starting condition used in Suselj et al. (2019a). In shallow convection, surface fluxes are the main driver for updraft surface conditions. Whether other physical processes are at play in the parameterization of updraft surface conditions in STBL should be investigated in the future. We find that in the current configuration, ED compensates for the overestimation of updraft moisture flux, resulting in a good match with LES in the total moisture flux.

Based on 800 additional simulations, exploring the parameter space, with different lateral entrainment rates and dynamical effects (varying L_0 and c_{ent} in Eq. 10 from and 10 to 100 m 0.5 to

5 m^{-1}, as well as varying z_{00} in Eq. 8 from 50 to 200 m; not shown), we observe that the most important impact of the updraft is the transport near cloud-top because ED models an insufficient heat and moisture transport in this location, causing a cold and moist bias. Additionally, ED does not accurately represent a well-mixed layer, while EDMF$_U$ has a better well-mixed profile in both θ_l and q_t. The final configuration was chosen to have the best match in the mean field of θ_l, q_t, and total heat and moisture transport with LES.

For EDMF$_{UD}$, Figure 7 shows partial contributions to the total transport from ED, updrafts, and downdrafts. Comparing Figures 6 and 7, we argue that the downdraft transport is implicitly included in the ED contribution in EDMF$_U$ (Figure 6A & D) as the sum of heat and moisture transport for EDMF$_U$ versus EDMF$_{UD}$ is similar. Averaged plume properties from EDMF$_{UD}$ are shown in Figure 8. For downdraft contribution to total fluxes, EDMF$_{UD}$ underestimates the strength in heat and moisture flux. More spefically, downdraft heat transport decreases too quickly before reaching the surface (Figure 7C). For moisture tansport, downdraft q_t also decrease quickly, and the starting downdraft q_t is underestimated (Figure 8C). Updraft contribution to heat transport (Figure 7B) is similar to that in EDMF$_U$, and they both slightly overestimate compared to LES in terms. This can be seen in the overestimation of updraft area and vertical velocity (Figure 8A, B), and is a result of the positive bias in updraft starting surface conditions, espicially updraft starting vertical velocity. For updraft moisture transport, updrafts in EDMF$_{UD}$ do not overestimate as strongly as EDMF$_U$. This is likely due to downdrafts transporting dry and warm air in the PBL and causing updrafts to mix differently. On top of that, the mean fields of θ_l and q_t are different in EDMF$_U$ and EDMF$_{UD}$. Note that since the definition of updrafts and downdrafts in LES is somewhat arbitrary, the total transport should be the main indicator of success for a parameterization. Nevertheless, the definition of updrafts and downdrafts as in Section 3 is a reference point for bench-marking updraft and downdraft parameterizations. Overall, general agreement of plume

properties are found between the SCMs and LES. For DYCOMS, downdraft transport decreases too quickly for both heat and moisture. We find that modeling downdraft transport in the upper part of the boundary layer correctly is more important than retaining downdraft throughout the PBL. The mean fields respond more to changes in turbulent transport in the upper part of the PBL. Indeed, the q_t profile is most well-mixed in EDMF$_{UD}$, signaling the importance of downdraft moisture transport. This is consistent with the hypothesis in Suselj et al. (2013), suggesting that the inclusion of downdrafts could increase vertical mixing in the upper part of the boundary layer. In STBL, mixing from the surface provides moisture and entrainment from the free troposphere dries the boundary layer. However, in the heat profile, both the surface and entrainment from the free troposphere heats the boundary layer. We find here that downdrafts help provide stronger moisture mixing near cloud-top and keep the bias in total moisture low. In addition, EDMF$_{UD}$ has the least bias in boundary layer averged θ_l, as downdrafts also contribute to transporting warm air in the PBL.

Downdraft model coefficients and final lateral entrainment configuration are chosen to have the best match against LES in the mean field of θ_l, q_t, u, and v. EDMF$_U$ and EDMF$_{UD}$ have the same updraft lateral entrainment configuration.

Comparing EDMF$_U$ with SCM results from Suselj et al. (2013), a resemblance of the updraft transport of heat and moisture is found. The formulations of updrafts are identical except for the added entrainment and dynamical pressure effect near cloud-top in EDMF$_U$. It is no surprise that some differences are seen, given the different assumptions made in ED. Specifically, the vertical transport in the middle of the boundary layer is different in the two models. While EDMF$_U$ shows positive transport from updraft in the cloudy region for heat, the updraft model in Suselj et al. (2013) shows a negative heat transport. For moisture, EDMF$_U$ produces stronger transport. This is likely due to the added entrainment dynamic effect in our updraft model, different subgrid cloud

assumption, and different ED model for the non-convective environment. In the end, the total heat and moisture transport is similar between the two models as ED compensates for the difference, and they both match LES well.

Comparing EDMF$_{UD}$ with SCM results from Han and Bretherton (2019), we found contrary conclusions for the effect of the downdraft parameterization. While Han and Bretherton (2019) found a slight overprediction for θ_l and overmixing for q_t in their DYCOMS experiment, we found slight underprediction for θ_l and undermixing for q_t.

b. CGILS S12 Control

Figure 9 shows the mean fields of θ_l, q_t, q_l, u, n, heat flux ($\rho c_p \overline{w'\theta_l'}$), and moisture flux ($\rho L_v \overline{w'q_t'}$) during hr 3 to 4, and the 24 h time series of liquid water path (LWP), boundary layer averaged heat (θ_l), and moisture (q_t) for the three tested PBL schemes are shown in Figure 10. ED shows a strong cold and moist bias throughout the entire simulation. For EDMF$_U$, boundary averaged heat and moisture both follow LES closely up to hr 10, then the moisture does not increase as much as in LES. Around hr 15, EDMF$_U$ begins to cool when compared to LES. This is likely a result of different radiation treatment used in LES and WRF. For EDMF$_{UD}$, similar trend is observed. Boundary layer averaged heat is warmer and moisture is direr than EDMF$_U$. Both EDMF$_U$ and EDMF$_{UD}$ match LWP in LES well. EDMF$_{UD}$ produces a slightly thinner cloud in the first half of the simulation, while EDMF$_U$ produces a slightly thicker cloud in the second half of the simulation.

During hr 3 to 4, EDMF$_U$ and EDMF$_{UD}$ show small bias in heat and moisture profile, whereas ED is too cold and too moist. This causes the overestimation of LWP in ED. The cloud-top height in EDMF$_{UD}$ is one grid point above ED, likely due to the stronger entrainment flux near cloud-top from mass-flux. EDMF$_{UD}$ overestimates u and underestimates v in the PBL. ED shows similar re-

sults as DYCOMS, where the horizontal wind does not have a strong transition between the PBL and the free troposphere. EDMF$_U$ shows a very good match in total heat and moisture transport, while EDMF$_{UD}$ has a slightly stronger moisture transport near cloud-top. Similar to DYCOMS, ED does not capture cloud-top entrainment flux. Figures 11 and 12 show the vertical flux contribution from each individual component: environment (ED), updrafts, and downdrafts. In both EDMF$_U$ and EDMF$_{UD}$, updraft heat and moisture transport are overestimated. However, in the presence of downdrafts, updraft moisture transport decreases more strongly in-cloud. Downdrafts in EDMF$_{UD}$ partially compensate these changes, resulting in a similar total transport. Averaged plume properties from EDMF$_{UD}$ are shown in Figure 13. In CGILS, good agreement of plume properties are found between the SCMs and LES. Again, we find that simulation results are more sensitive to the modeling of downdraft transport in the upper part of the PBL. In the end, we select model parameters that result in good mean field of θ_l, q_t, u, and v for both DYCOMS and CGILS. While downdrafts terminate too quickly in DYCOMS, we find that they mostly reach the surface in CGILS.

In the present study, we develop our updraft and downdraft parameterization using their nocturnal properties. The 24 h simulation of CGILS suggests that updrafts and downdrafts may play different roles during the day time. This is also observed in the study done by Brient et al. (2019). Parameterization of updrafts and downdrafts during the day should be investigated in the future.

c. Simulation time step and run-time

We test the simulation with different time steps: 5, 10, 20, 30, and 40 s as shown in Fig 14. Results suggest that both EDMF$_U$ and EDMF$_{UD}$ are not sensitive to time step. LWP, and boundary layer averaged heat and moisture all converge to the same value at the end of the simulation. The figures shown in this study use a time step of 40 s. Additionally, we record simulation run time

normalized by ED for different time steps in Table 2. On average, including updrafts slows the simulation by 5%, while including both updrafts and downdrafts slows the simulation by 7%.

5. Summary and conclusions

In this study, we investigated the role of non-local transport on the development and maintenance of the STBL in coarse-resolution atmospheric models. A special emphasis has been put on the evaluation of the downdraft contribution, recently suggested as an important missing element of convection/turbulence parameterizations (Chinita et al. 2017; Davini et al. 2017; Brient et al. 2019) and implemented in a different atmospheric model that uses different eddy-diffusivity and mass-flux models (Han and Bretherton 2019). A new parameterization of cloud-top triggered downdrafts has been proposed and validated, along with a complementary parameterization of surface-driven updrafts, against large-eddy simulations of two marine stratocumulus cases: DYCOMS and CGILS. The applied non-local mass-flux scheme is part of the stochastic multi-plume EDMF approach decomposing the turbulence into the local and non-local contributions. The local transport in the boundary layer is represented by the MYNN scheme. The EDMF scheme has been implemented in the WRF single-column modeling framework.

The thermodynamic and dynamic properties of downdrafts are governed by stochastic lateral entrainment and the difference from the mean properties of the environment. The number of downdrafts is fixed to 10 for a time step of 40 s, and all downdrafts are assumed to start randomly in upper half of the cloud layer, with a starting area of approximately 15%. The strength of the downdraft vertical velocity is formulated as a combined effect of the intensity of the surface-driven updrafts and cloud-top radiative cooling. The starting downdraft thermodynamic properties are proportional to the entrainment flux, which is determined by the jump values of heat or moisture across the inversion.

To evaluate the importance of the updraft and downdraft contributions, we run three different SCM simulations for each case: without mass flux (ED), with updrafts only (EDMF$_U$), and with both updrafts and downdrafts (EDMF$_{UD}$). When there is no mass-flux (neither updraft nor downdraft), ED underestimates the cloud-top entrainment flux, resulting in a cold and moist bias that leads to a strong overestimation of LWP. Including updrafts increases the cloud-top entrainment flux and keeps the mean profile more well-mixed and warmer and drier. We find that including downdrafts increases vertical mixing in the upper part of the boundary layer especially in q_t, and it results in warmer and drier PBL than EDMF$_U$. Overall, the parameterization reproduces the LES profiles because of the addition of downdraft heat and moisture transport in the WRF SCM. However, we find that differences in EDMF$_U$ and EDMF$_{UD}$ are not significant.

Based on the two STBL cases, we conclude that it is necessary to include updrafts as part of the non-local mass-flux as ED does not capture the cloud-top entrainment flux. The addition of downdrafts shows some improvements in these two cases. However, further investigations are needed to determine whether downdrafts play greater roles in different meteorological conditions. We hypothesize that ED would have a better match with LES when there is less cloud-top entrainment (e.g., when the PBL is less turbulent), and that the inclusion of downdrafts would be necessary when surface fluxes are small. A recent study by Matheou and Teixeira (2019) performed various LES of STBL with different physical and numerical model parameters and concluded that surface fluxes, surface shear, and cloud-top radiative cooling all contribute substantially to the turbulence in STBL. Whether the EDMF parameterization responds similarly in such conditions will be investigated in the future.

Acknowledgments. Parts of this research were carried out at the Jet Propulsion Laboratory, California Institute of Technology, under a contract with the National Aeronautics and Space Ad-

ministration, and were supported by the U.S. Department of Energy, Office of Biological and Environmental Research, Earth System Modeling; and the NASA MAP Program. E. Wu acknowledges the support provided by the JPL Education Office. We would like to thank Mónica Zamora Zapata and Thijs Heus for constructive comments. We also thank Minghua Ong for proofreading the manuscript. The WRF model is freely available at `https://github.com/wrf-model/WRF`, the modifications made in this paper can be found at `https://github.com/elynnwu/EDMF_JPL`.

References

Angevine, W. M., H. Jiang, and T. Mauritsen, 2010: Performance of an Eddy Diffusivity–Mass Flux Scheme for Shallow Cumulus Boundary Layers. *Mon. Wea. Rev.*, **138 (7)**, 2895–2912, doi:10.1175/2010MWR3142.1.

Angevine, W. M., J. Olson, J. Kenyon, W. I. Gustafson, S. Endo, K. Suselj, and D. D. Turner, 2018: Shallow Cumulus in WRF Parameterizations Evaluated against LASSO Large-Eddy Simulations. *Mon. Wea. Rev.*, **146 (12)**, 4303–4322, doi:10.1175/MWR-D-18-0115.1.

Benjamin, S. G., and Coauthors, 2016: A North American Hourly Assimilation and Model Forecast Cycle: The Rapid Refresh. *Mon. Wea. Rev.*, **144 (4)**, 1669–1694, doi:10.1175/MWR-D-15-0242.1.

Blossey, P. N., and Coauthors, 2013: Marine low cloud sensitivity to an idealized climate change: The CGILS LES intercomparison. *J. Adv. Model. Earth Syst.*, **5 (2)**, 234–258, doi:10.1002/jame.20025.

Bony, S., and J.-L. Dufresne, 2005: Marine boundary layer clouds at the heart of tropical cloud feedback uncertainties in climate models. *Geophys. Res. Lett.*, **32 (20)**, doi:10.1029/2005GL023851.

Brient, F., F. Couvreux, N. Villefranque, C. Rio, and R. Honnert, 2019: Object-Oriented Identification of Coherent Structures in Large Eddy Simulations: Importance of Downdrafts in Stratocumulus. *Geophys. Res. Lett.*, **46 (5)**, 2854–2864, doi:10.1029/2018GL081499.

Chinita, M. J., G. Matheou, and J. Teixeira, 2017: A Joint Probability Density–Based Decomposition of Turbulence in the Atmospheric Boundary Layer. *Mon. Wea. Rev.*, **146 (2)**, 503–523, doi:10.1175/MWR-D-17-0166.1.

Chung, D., G. Matheou, and J. Teixeira, 2012: Steady-State Large-Eddy Simulations to Study the Stratocumulus to Shallow Cumulus Cloud Transition. *J. Atmos. Sci.*, **69 (11)**, 3264–3276, doi:10.1175/JAS-D-11-0256.1.

Crosbie, E., and Coauthors, 2016: Stratocumulus Cloud Clearings and Notable Thermodynamic and Aerosol Contrasts across the Clear–Cloudy Interface. *J. Atmos. Sci.*, **73 (3)**, 1083–1099, doi:10.1175/JAS-D-15-0137.1.

Davini, P., F. D'Andrea, S.-B. Park, and P. Gentine, 2017: Coherent Structures in Large-Eddy Simulations of a Nonprecipitating Stratocumulus-Topped Boundary Layer. *J. Atmos. Sci.*, **74 (12)**, 4117–4137, doi:10.1175/JAS-D-17-0050.1.

de Lozar, A., and J. P. Mellado, 2015: Mixing Driven by Radiative and Evaporative Cooling at the Stratocumulus Top. *J. Atmos. Sci.*, **72 (12)**, 4681–4700, doi:10.1175/JAS-D-15-0087.1.

de Roode, S. R., A. P. Siebesma, H. J. J. Jonker, and Y. de Voogd, 2012: Parameterization of the Vertical Velocity Equation for Shallow Cumulus Clouds. *Mon. Wea. Rev.*, **140 (8)**, 2424–2436, doi:10.1175/MWR-D-11-00277.1.

Engström, A., F. A.-M. Bender, and J. Karlsson, 2014: Improved Representation of Marine Stratocumulus Cloud Shortwave Radiative Properties in the CMIP5 Climate Models. *J. Climate*, **27 (16)**, 6175–6188, doi:10.1175/JCLI-D-13-00755.1.

Gerber, H., G. Frick, S. P. Malinowski, J.-L. Brenguier, and F. Burnet, 2005: Holes and Entrainment in Stratocumulus. *J. Atmos. Sci.*, **62 (2)**, 443–459, doi:10.1175/JAS-3399.1.

Ghonima, M. S., H. Yang, C. K. Kim, T. Heus, and J. Kleissl, 2017: Evaluation of WRF SCM Simulations of Stratocumulus-Topped Marine and Coastal Boundary Layers and Improvements to Turbulence and Entrainment Parameterizations. *J. Adv. Model. Earth Syst.*, **9 (7)**, 2635–2653, doi:10.1002/2017MS001092.

Hahn, C., and S. Warren, 2007: A Gridded Climatology of Clouds over Land (1971-96) and Ocean (1954-97) from Surface Observations Worldwide. Numeric Data Package NDP–026E ORNL/CDIAC–153, CDIAC, Department of Energy, Oak Ridge, TN., doi:10.3334/CDIAC/cli.ndp026e.

Han, J., and C. S. Bretherton, 2019: TKE-Based Moist Eddy-Diffusivity Mass-Flux (EDMF) Parameterization for Vertical Turbulent Mixing. *Wea. Forecasting*, **34 (4)**, 869–886, doi:10.1175/WAF-D-18-0146.1.

Hong, S.-Y., Y. Noh, and J. Dudhia, 2006: A New Vertical Diffusion Package with an Explicit Treatment of Entrainment Processes. *Mon. Wea. Rev.*, **134 (9)**, 2318–2341, doi:10.1175/MWR3199.1, iSBN: 0027-0644.

Huang, H.-Y., A. Hall, and J. Teixeira, 2013: Evaluation of the WRF PBL Parameterizations for Marine Boundary Layer Clouds: Cumulus and Stratocumulus. *Mon. Wea. Rev.*, **141 (7)**, 2265–2271, doi:10.1175/MWR-D-12-00292.1.

Iacono, M. J., J. S. Delamere, E. J. Mlawer, M. W. Shephard, S. A. Clough, and W. D. Collins, 2008: Radiative forcing by long-lived greenhouse gases: Calculations with the AER radiative transfer models. *J. Geophys. Res.*, **113 (D13)**, doi:10.1029/2008JD009944.

Kurowski, M. J., S. P. Malinowski, and W. W. Grabowski, 2009: A numerical investigation of entrainment and transport within a stratocumulus-topped boundary layer. *Quart. J. Roy. Meteor. Soc.*, **135 (638)**, 77–92, doi:10.1002/qj.354.

Kuwano-Yoshida, A., T. Enomoto, and W. Ohfuchi, 2010: An improved PDF cloud scheme for climate simulations. *Quart. J. Roy. Meteor. Soc.*, **136 (651)**, 1583–1597, doi:10.1002/qj.660, URL https://rmets.onlinelibrary.wiley.com/doi/abs/10.1002/qj.660.

Köhler, M., 2006: An integral approach to modeling PBL transports and clouds: EDMF@ECMWF. *Proceedings of workshop on parametrization of clouds in large-scale models*, 13–15 November 2006. ECMWF: Reading, UK. 93–101.

Lilly, D. K., 1968: Models of cloud-topped mixed layers under a strong inversion. *Quart. J. Roy. Meteor. Soc.*, **94 (401)**, 292–309, doi:10.1002/qj.49709440106.

Lin, J.-L., T. Qian, and T. Shinoda, 2014: Stratocumulus Clouds in Southeastern Pacific Simulated by Eight CMIP5–CFMIP Global Climate Models. *J. Climate*, **27 (8)**, 3000–3022, doi:10.1175/JCLI-D-13-00376.1.

Lock, A. P., and M. K. Macvean, 1999: The parametrization of entrainment driven by surface heating and cloud-top cooling. *Quart. J. Roy. Meteor. Soc.*, **125 (553)**, 271–299, doi:10.1002/qj.49712555315.

Malinowski, S. P., and Coauthors, 2013: Physics of Stratocumulus Top (POST): Turbulent mixing across capping inversion. *Atmos. Chem. Phys.*, **13 (24)**, 12 171–12 186, doi:10.5194/acp-13-12171-2013.

Matheou, G., and J. Teixeira, 2019: Sensitivity to physical and numerical aspects of large-eddy simulation of stratocumulus. *Mon. Wea. Rev.*, doi:10.1175/MWR-D-18-0294.1.

Mellado, J. P., 2017: Cloud-Top Entrainment in Stratocumulus Clouds. *Annu. Rev. Fluid Mech*, **49**, 145–69, doi:10.1146/annurev-fluid-010816-060231.

Mellado, J. P., C. S. Bretherton, B. Stevens, and M. C. Wyant, 2018: DNS and LES for Simulating Stratocumulus: Better Together. *J. Adv. Model. Earth Syst.*, **10 (7)**, 1421–1438, doi:10.1029/2018MS001312.

Mellado, J. P., B. Stevens, and H. Schmidt, 2014: Wind Shear and Buoyancy Reversal at the Top of Stratocumulus. *J. Atmos. Sci.*, **71 (3)**, 1040–1057, doi:10.1175/JAS-D-13-0189.1.

Mellor, G. L., and T. Yamada, 1982: Development of a turbulence closure model for geophysical fluid problems. *Rev. Geophys. Space Phys.*, **20 (4)**, 851–875, doi:10.1029/RG020i004p00851.

Nakanishi, M., and H. Niino, 2006: An Improved Mellor–Yamada Level-3 Model: Its Numerical Stability and Application to a Regional Prediction of Advection Fog. *Bound.-Layer Meteor*, **119 (2)**, 397–407, doi:10.1007/s10546-005-9030-8.

Nakanishi, M., and H. Niino, 2009: Development of an Improved Turbulence Closure Model for the Atmospheric Boundary Layer. . *J. Meteor. Soc. Japan*, **87 (5)**, 895–912, doi:10.2151/jmsj.87.895.

Neggers, R. A. J., 2009: A Dual Mass Flux Framework for Boundary Layer Convection. Part II: Clouds. *J. Atmos. Sci.*, **66 (6)**, 1489–1506, doi:10.1175/2008JAS2636.1.

Neggers, R. A. J., M. Kohler, and A. C. M. Beljaars, 2009: A Dual Mass Flux Framework for Boundary Layer Convection. Part I: Transport. *J. Atmos. Sci.*, **66 (6)**, 1465–1487, doi:10.1175/2008JAS2635.1.

Olson, J. B., J. S. Kenyon, W. A. Angevine, J. M. Brown, M. Pagowski, and K. Sušelj, 2019: A Description of the MYNN-EDMF Scheme and the Coupling to Other Components in WRF–ARW. *NOAA Technical Memorandum OAR GSD-61*, doi:10.25923/n9wm-be49.

Pedersen, J. G., S. P. Malinowski, and W. W. Grabowski, 2016: Resolution and domain-size sensitivity in implicit large-eddy simulation of the stratocumulus-topped boundary layer. *J. Adv. Model. Earth Syst.*, **8 (2)**, 885–903, doi:10.1002/2015MS000572.

Pincus, R., and B. Stevens, 2009: Monte Carlo Spectral Integration: a Consistent Approximation for Radiative Transfer in Large Eddy Simulations: MONTE CARLO SPECTRAL INTEGRATION. *J. Adv. Model. Earth Syst.*, **1 (2)**, n/a–n/a, doi:10.3894/JAMES.2009.1.1.

Pleim, J. E., 2007: A Combined Local and Nonlocal Closure Model for the Atmospheric Boundary Layer. Part I: Model Description and Testing. *J. Appl. Meteor. Climatol.*, **46 (9)**, 1383–1395, doi:10.1175/JAM2539.1.

Reynolds, D. W., D. A. Clark, F. W. Wilson, and L. Cook, 2012: Forecast-Based Decision Support for San Francisco International Airport: A NextGen Prototype System That Improves Operations during Summer Stratus Season. *Bull. Amer. Meteor. Soc.*, **93 (10)**, 1503–1518, doi:10.1175/BAMS-D-11-00038.1.

Siebesma, A. P., P. M. M. Soares, and J. Teixeira, 2007: A Combined Eddy-Diffusivity Mass-Flux Approach for the Convective Boundary Layer. *J. Atmos. Sci.*, **64 (4)**, 1230–1248, doi:10.1175/JAS3888.1.

Siebesma, A. P., and J. Teixeira, 2000: An Advection-Diffusion scheme for the convective boundary layer: description and 1d-results. *14th Symp. on Boundary Layers and Turbulence*, Aspen, CO, Amer. Meteor. Soc., 231–234., URL https://ams.confex.com/ams/AugAspen/techprogram/paper_14840.htm.

Soares, P. M. M., P. M. A. Miranda, A. P. Siebesma, and J. Teixeira, 2004: An eddy-diffusivity/mass-flux parametrization for dry and shallow cumulus convection. *Quart. J. Roy. Meteor. Soc.*, **130 (604)**, 3365–3383, doi:10.1256/qj.03.223.

Stevens, B., 2002: Entrainment in stratocumulus-topped mixed layers. *Quart. J. Roy. Meteor. Soc.*, **128 (586)**, 2663–2690, doi:10.1256/qj.01.202.

Stevens, B., 2010: Introduction to UCLA-LES. URL https://www.mpimet.mpg.de/fileadmin/atmosphaere/herz/les_doc.pdf.

Stevens, B., and Coauthors, 2003: Dynamics and Chemistry of Marine Stratocumulus—DYCOMS-II. *Bull. Amer. Meteor. Soc.*, **84 (5)**, 579–594, doi:10.1175/BAMS-84-5-579.

Stevens, B., and Coauthors, 2005: Evaluation of Large-Eddy Simulations via Observations of Nocturnal Marine Stratocumulus. *Mon. Wea. Rev.*, **133 (6)**, 1443–1462, doi:10.1175/MWR2930.1.

Suselj, K., M. J. Kurowski, and J. Teixeira, 2019a: On the Factors Controlling the Development of Shallow Convection in Eddy-Diffusivity/Mass-Flux Models. *J. Atmos. Sci.*, **76 (2)**, 433–456, doi:10.1175/JAS-D-18-0121.1.

Suselj, K., M. J. Kurowski, and J. Teixeira, 2019b: A Unified Eddy-Diffusivity/Mass-Flux Approach for Modeling Atmospheric Convection. *J. Atmos. Sci.*, **76 (8)**, 2505–2537, doi:10.1175/JAS-D-18-0239.1.

Suselj, K., J. Teixeira, and D. Chung, 2013: A Unified Model for Moist Convective Boundary Layers Based on a Stochastic Eddy-Diffusivity/Mass-Flux Parameterization. *J. Atmos. Sci.*, **70 (7)**, 1929–1953, doi:10.1175/JAS-D-12-0106.1.

Teixeira, J., 1999: Simulation of fog with the ECMWF prognostic cloud scheme. *Quart. J. Roy. Meteor. Soc.*, **125 (554)**, 529–552, doi:10.1002/qj.49712555409.

Teixeira, J., and A. P. Siebesma, 2000: A Mass-Flux/K-Diffusion approach to the parameterization of the convective boundary layer: global model results. *14th Symp. on Boundary Layers and Turbulence*, Aspen, CO, Amer. Meteor. Soc., 231–234., URL https://ams.confex.com/ams/AugAspen/techprogram/paper_14915.htm.

Teixeira, J., and Coauthors, 2011: Tropical and Subtropical Cloud Transitions in Weather and Climate Prediction Models: The GCSS/WGNE Pacific Cross-Section Intercomparison (GPCI). *J. Climate*, **24 (20)**, 5223–5256, doi:10.1175/2011JCLI3672.1.

Witek, M. L., J. Teixeira, and G. Matheou, 2011: An Integrated TKE-Based Eddy Diffusivity/Mass Flux Boundary Layer Closure for the Dry Convective Boundary Layer. *J. Atmos. Sci.*, **68 (7)**, 1526–1540, doi:10.1175/2011JAS3548.1.

Wood, R., 2012: Stratocumulus Clouds. *Mon. Wea. Rev.*, **140 (8)**, 2373–2423, doi:10.1175/MWR-D-11-00121.1.

Wood, R., and C. S. Bretherton, 2006: On the Relationship between Stratiform Low Cloud Cover and Lower-Tropospheric Stability. *J. Climate*, **19 (24)**, 6425–6432, doi:10.1175/JCLI3988.1.

Wu, E., R. E. S. Clemesha, and J. Kleissl, 2018: Coastal Stratocumulus cloud edge forecasts. *Sol. Energy*, **164**, 355–369, doi:10.1016/j.solener.2018.02.072, URL https://doi.org/10.1016/j.solener.2018.02.072.

727 Yamaguchi, T., and D. A. Randall, 2011: Cooling of Entrained Parcels in a Large-Eddy Simula-
728 tion. *J. Atmos. Sci.*, **69 (3)**, 1118–1136, doi:10.1175/JAS-D-11-080.1.

729 Yang, H., and J. Kleissl, 2016: Preprocessing WRF initial conditions for coastal stratocumulus
730 forecasting. *Sol. Energy*, **133**, 180–193, doi:10.1016/j.solener.2016.04.003.

731 Zelinka, M. D., D. A. Randall, M. J. Webb, and S. A. Klein, 2017: Clearing clouds of uncertainty.
732 *Nat. Climate Change*, **7**, 674–678, doi:10.1038/nclimate3402.

733 Zhong, X., D. K. Sahu, and J. Kleissl, 2017: WRF inversion base height ensembles for simulating
734 marine boundary layer stratocumulus. *Sol. Energy*, **146**, 50–64, doi:10.1016/j.solener.2017.02.
735 021.

LIST OF TABLES

Table 1. Summary of large eddy simulation setups in UCLA-LES, including uniform horizontal grid spacing $\Delta x, y$, vertical grid spacing at the inversion $\Delta z_{inv}[m]$, horizontal domain size $L_{x,y}$, and divergence of large-scale winds D. 37

Table 2. EDMF$_U$ and EDMF$_{UD}$ run time normalized by ED using different time steps. . . 38

TABLE 1. Summary of large eddy simulation setups in UCLA-LES, including uniform horizontal grid spacing $\Delta x, y$, vertical grid spacing at the inversion $\Delta z_{inv}[m]$, horizontal domain size $L_{x,y}$, and divergence of large-scale winds D.

Case	$\Delta x, y[m]$	$\Delta z_{inv}[m]$	z_{inv}	$L_{x,y}[m]$	$L_z[m]$	$D[s^{-1}]$
DYCOMS-II RF01	35	5	837	3,360	1568	3.75×10^{-6}
CGILS S12 Control	25	5	677	2,400	1572	1.68×10^{-6}

TABLE 2. EDMF$_U$ and EDMF$_{UD}$ run time normalized by ED using different time steps.

Time step [s]	5	10	20	30	40	Avg
EDMF$_U$	1.07	1.01	1.02	1.11	1.04	1.05
EDMF$_{UD}$	1.10	1.01	1.04	1.10	1.08	1.07

LIST OF FIGURES

Fig. 1. Joint probability density function (PDF) of normalized vertical velocity fluctuations w' and (A) normalized total mixing ratio fluctuations q_t', (B) normalized virtual potential temperature fluctuations θ_v', and (C) normalized liquid water potential temperature fluctuations θ_l' near cloud-top ($z/z_i = 0.97$). Each tick represents one standard deviation away from the mean. LES results from hour 3-4 are shown. 41

Fig. 2. DYCOMS case: Updraft and downdraft area (A), vertical velocity (D), difference from mean liquid water potential temperature (E), virtual potential temperature (F), total water mixing ratio (G), and actual liquid water mixing ratio (H). (B) and (C) show the contribution to total heat and moisture flux from updrafts, downdrafts, and the environment. For this and all following figures, WRF results from hour 3-4 are shown. 42

Fig. 3. CGILS case: Updraft and downdraft area (A), vertical velocity (D), difference from mean liquid water potential temperature (E), virtual potential temperature (F), total water mixing ratio (G), and actual liquid water mixing ratio (H). (B) and (C) show the contribution to total heat and moisture flux from updrafts, downdrafts, and the environment. 43

Fig. 4. DYCOMS case: WRF SCM hour 3-4 averaged results for mean field of liquid water potential temperature (A), total water mixing ratio (B), liquid water mixing ratio (C), cloud fraction (D), zonal wind (E), meridional wind (F), total heat flux (E), and total moisture flux (H). The black line is the result from UCLA-LES, while the shaded range is from an LES inter-comparison study Stevens et al. (2005). Note that gird-mean liquid water mixing ratio is calculated using a statistical partial condensation ($bl\_mynn\_cloudpdf = 1$), the condensation routine is called at the end of PBL scheme after mixing from both ED and MF are completed. 44

Fig. 5. DYCOMS case: time series of liquid water path, boundary layer averaged heat (θ_l), and moisture (q_t). 45

Fig. 6. DYCOMS case: WRF SCM heat and moisture flux contribution from eddy diffusivity (A and D), updraft mass flux (B and E), and total flux (C and F). 46

Fig. 7. DYCOMS case: WRF SCM heat and moisture flux contribution from eddy diffusivity (A and E), updraft mass flux (B and F), downdraft mass flux (C and G), and total flux (D and H). . 47

Fig. 8. DYCOMS case: WRF EDMF$_{UD}$ plume properties of (A) area, (B) vertical velocity perturbations, (C) total water mixing ratio perturbations, (D) liquid water potential temperature perturbations, (E) virtual potential temperature perturbations, and (F) liquid water content for both updraft (red solid) and downdraft (blue dashed). LES results as in Fig 2 are in solid dark (updraft) and dashed dark (downdraft) line. 48

Fig. 9. CGILS case: WRF SCM hour 3-4 averaged results for mean field of liquid water potential temperature (A), total water mixing ratio (B), liquid water mixing ratio (C), cloud fraction (D), zonal wind (E), meridional wind (F), total heat flux (E), and total moisture flux (H). . . 49

Fig. 10. CGILS case: time series of liquid water path, boundary layer averaged heat (θ_l), and moisture (q_t). 50

Fig. 11. CGILS case: WRF SCM heat and moisture flux contribution from eddy diffusivity (A and D), updraft mass flux (B and E), and total flux (C and F). 51

Fig. 12. CGILS case: WRF SCM heat and moisutre flux from individual component– eddy diffusivity (A and E), updraft mass flux (B and F), downdraft mass flux (C and G), and total flux (D and H). 52

Fig. 13. CGILS case: WRF EDMF$_{UD}$ plume properties of (A) area, (B) vertical velocity perturbations, (C) total water mixing ratio perturbations, (D) liquid water potential temperature perturbations, (E) virtual potential temperature perturbations, and (F) liquid water content for both updraft (red solid) and downdraft (blue dashed). LES results as in Fig 3 are in solid dark (updraft) and dashed dark (downdraft) line. 53

Fig. 14. Simulation results using different time step in EDMF$_U$ and EDMF$_{UD}$ for both DYCOMS and CGILS. 54

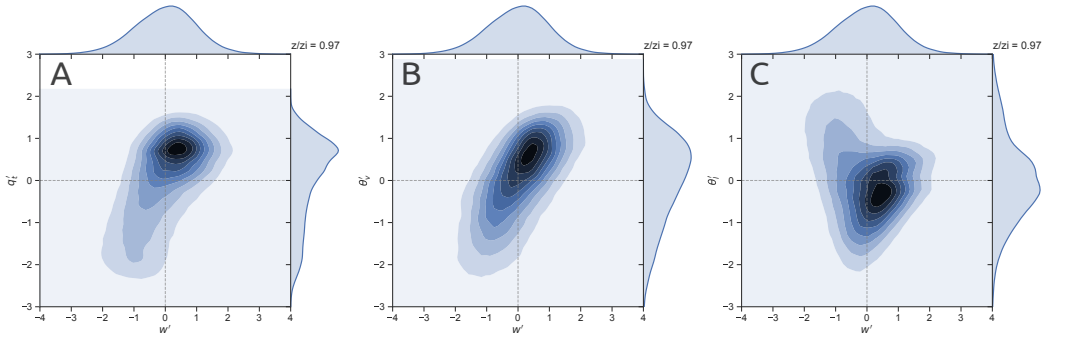

FIG. 1. Joint probability density function (PDF) of normalized vertical velocity fluctuations w' and (A) normalized total mixing ratio fluctuations q_t', (B) normalized virtual potential temperature fluctuations θ_v', and (C) normalized liquid water potential temperature fluctuations θ_l' near cloud-top $(z/z_i = 0.97)$. Each tick represents one standard deviation away from the mean. LES results from hour 3-4 are shown.

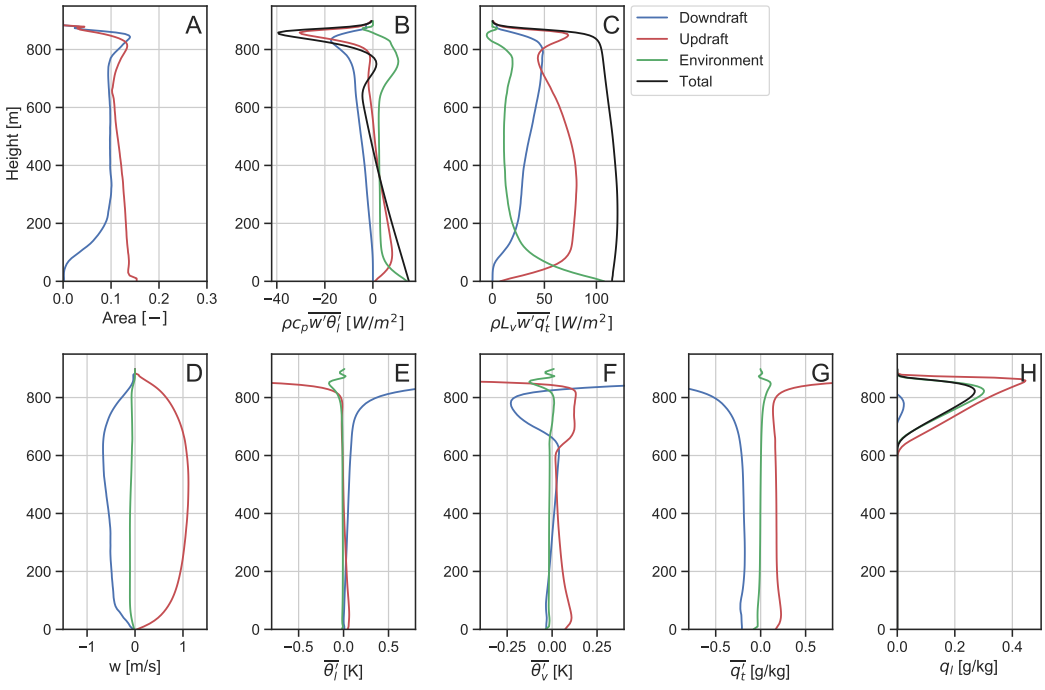

FIG. 2. DYCOMS case: Updraft and downdraft area (A), vertical velocity (D), difference from mean liquid water potential temperature (E), virtual potential temperature (F), total water mixing ratio (G), and actual liquid water mixing ratio (H). (B) and (C) show the contribution to total heat and moisture flux from updrafts, downdrafts, and the environment. For this and all following figures, WRF results from hour 3-4 are shown.

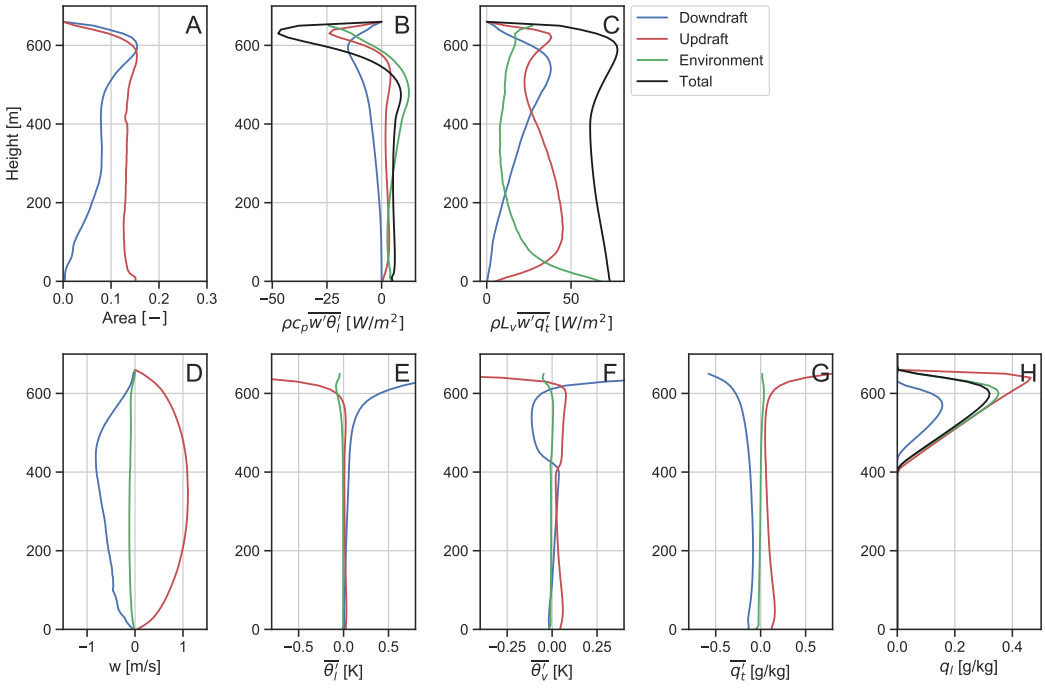

FIG. 3. CGILS case: Updraft and downdraft area (A), vertical velocity (D), difference from mean liquid water potential temperature (E), virtual potential temperature (F), total water mixing ratio (G), and actual liquid water mixing ratio (H). (B) and (C) show the contribution to total heat and moisture flux from updrafts, downdrafts, and the environment.

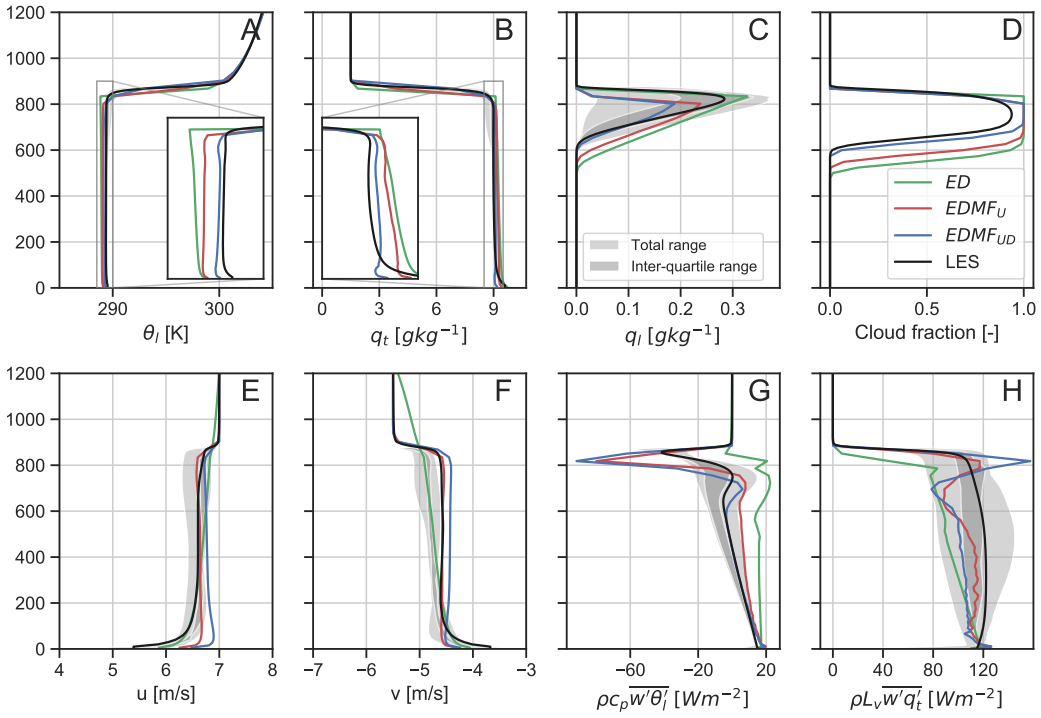

FIG. 4. DYCOMS case: WRF SCM hour 3-4 averaged results for mean field of liquid water potential temperature (A), total water mixing ratio (B), liquid water mixing ratio (C), cloud fraction (D), zonal wind (E), meridional wind (F), total heat flux (E), and total moisture flux (H). The black line is the result from UCLA-LES, while the shaded range is from an LES inter-comparison study Stevens et al. (2005). Note that gird-mean liquid water mixing ratio is calculated using a statistical partial condensation ($bl\_mynn\_cloudpdf = 1$), the condensation routine is called at the end of PBL scheme after mixing from both ED and MF are completed.

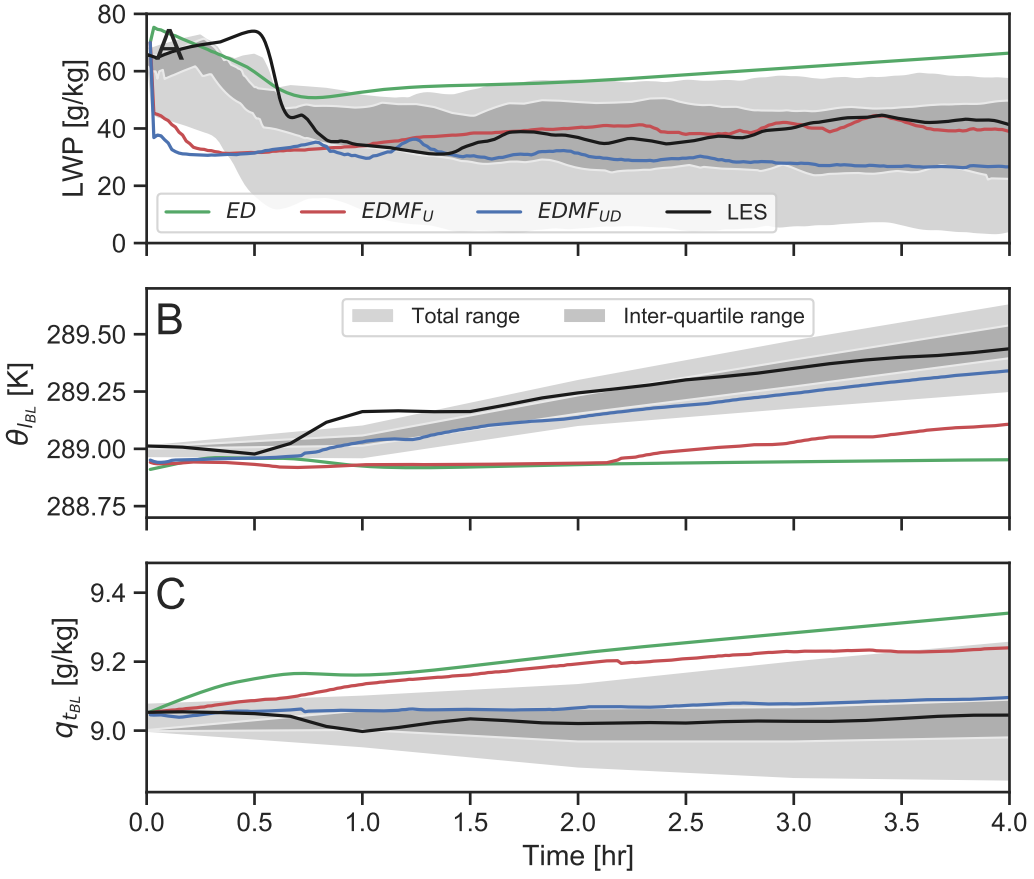

FIG. 5. DYCOMS case: time series of liquid water path, boundary layer averaged heat (θ_l), and moisture (q_t).

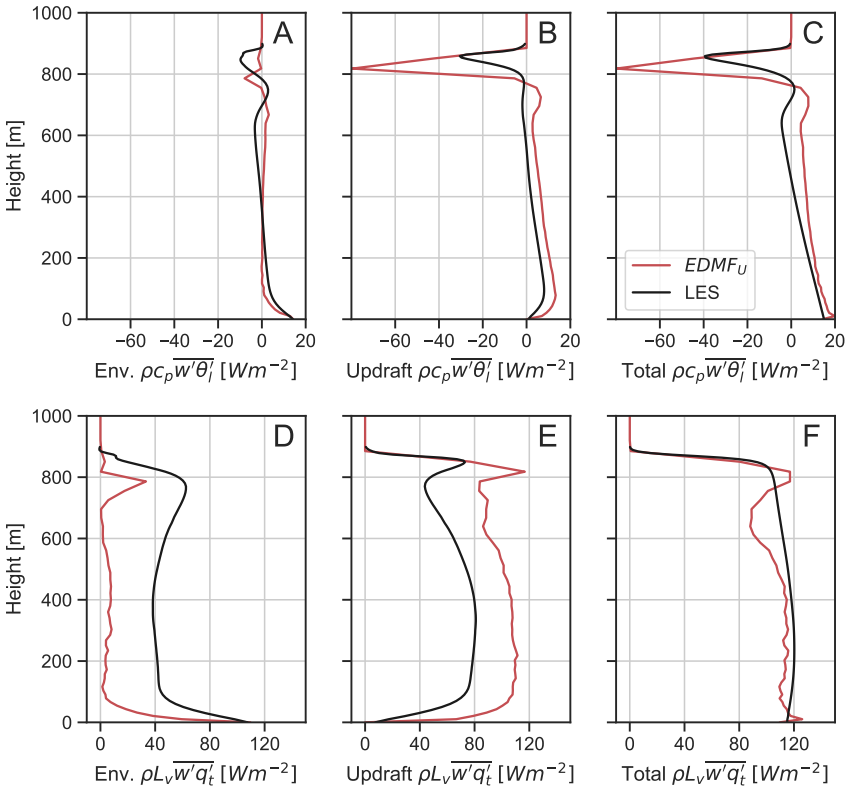

FIG. 6. DYCOMS case: WRF SCM heat and moisture flux contribution from eddy diffusivity (A and D), updraft mass flux (B and E), and total flux (C and F).

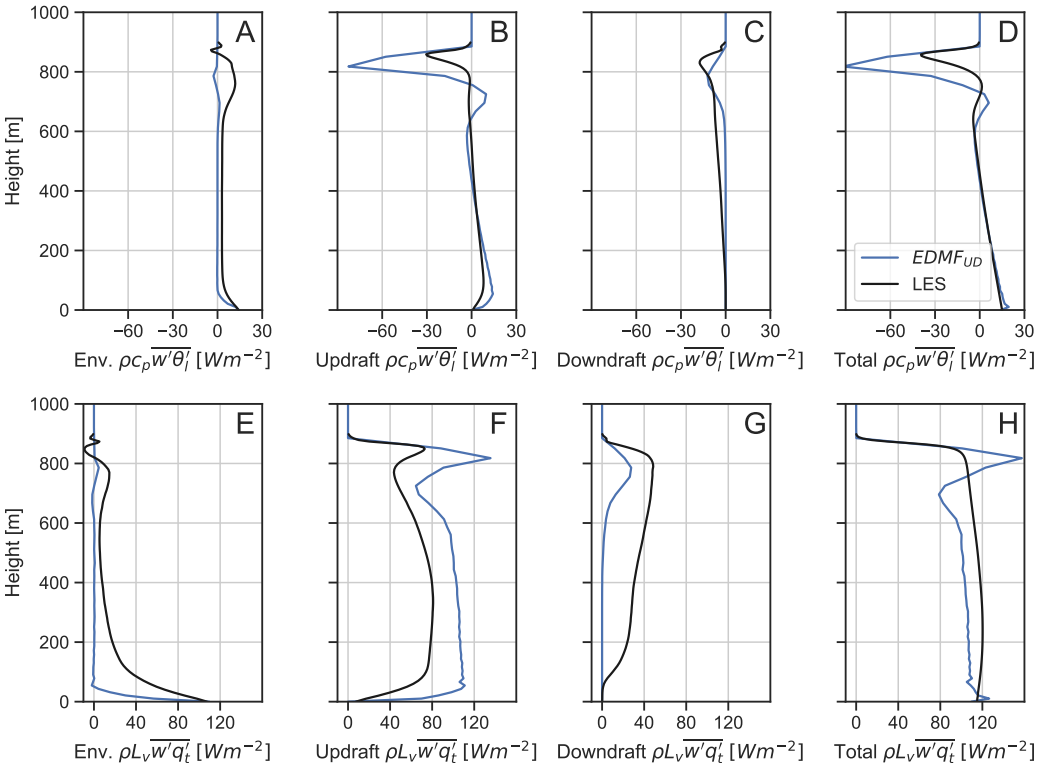

815 FIG. 7. DYCOMS case: WRF SCM heat and moisture flux contribution from eddy diffusivity (A and E),
816 updraft mass flux (B and F), downdraft mass flux (C and G), and total flux (D and H).

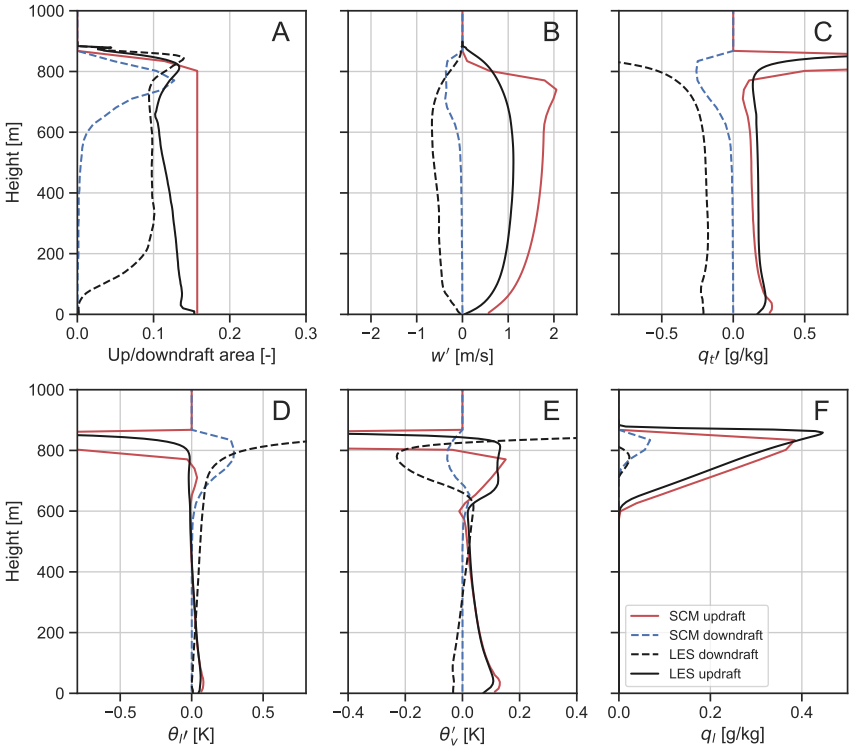

FIG. 8. DYCOMS case: WRF EDMF$_{UD}$ plume properties of (A) area, (B) vertical velocity perturbations, (C) total water mixing ratio perturbations, (D) liquid water potential temperature perturbations, (E) virtual potential temperature perturbations, and (F) liquid water content for both updraft (red solid) and downdraft (blue dashed). LES results as in Fig 2 are in solid dark (updraft) and dashed dark (downdraft) line.

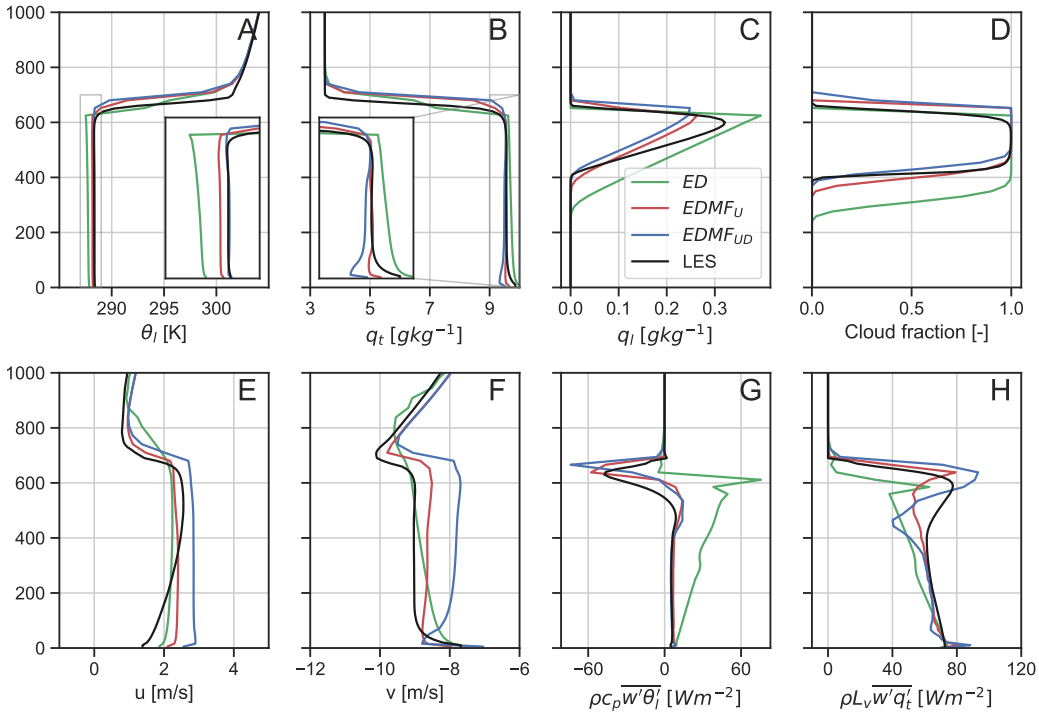

821 FIG. 9. CGILS case: WRF SCM hour 3-4 averaged results for mean field of liquid water potential temperature
822 (A), total water mixing ratio (B), liquid water mixing ratio (C), cloud fraction (D), zonal wind (E), meridional
823 wind (F), total heat flux (E), and total moisture flux (H).

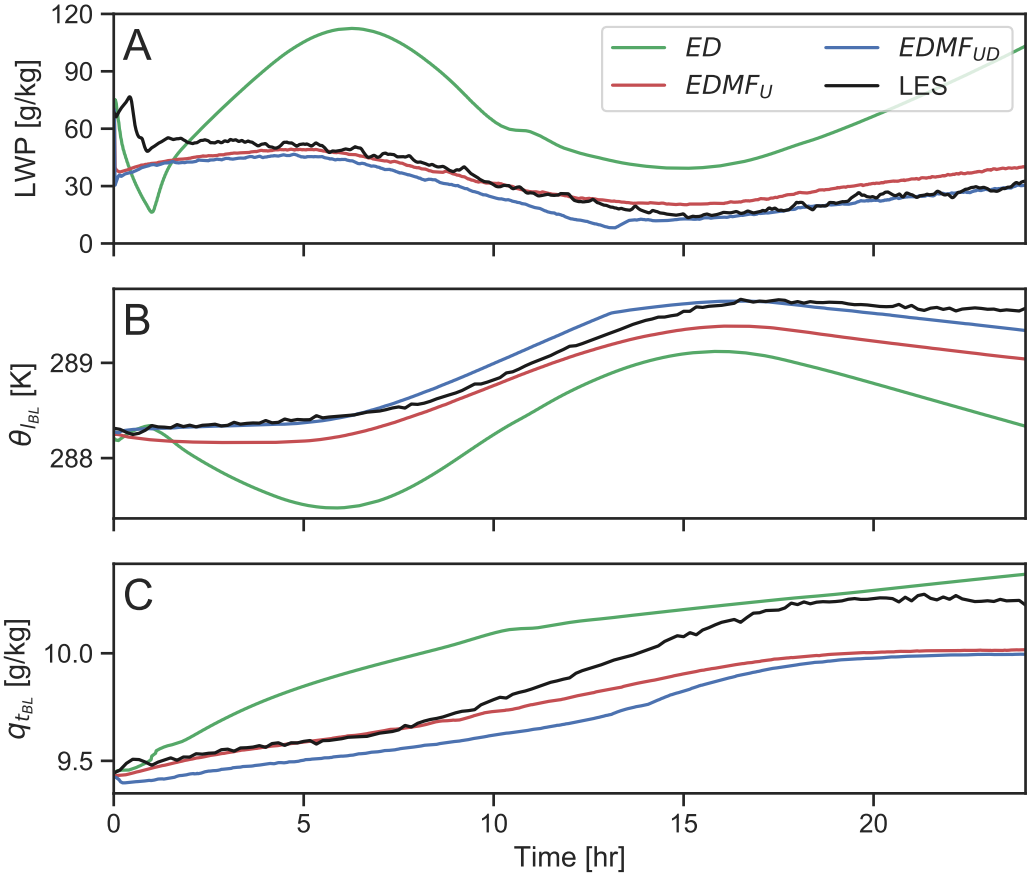

FIG. 10. CGILS case: time series of liquid water path, boundary layer averaged heat (θ_l), and moisture (q_t).

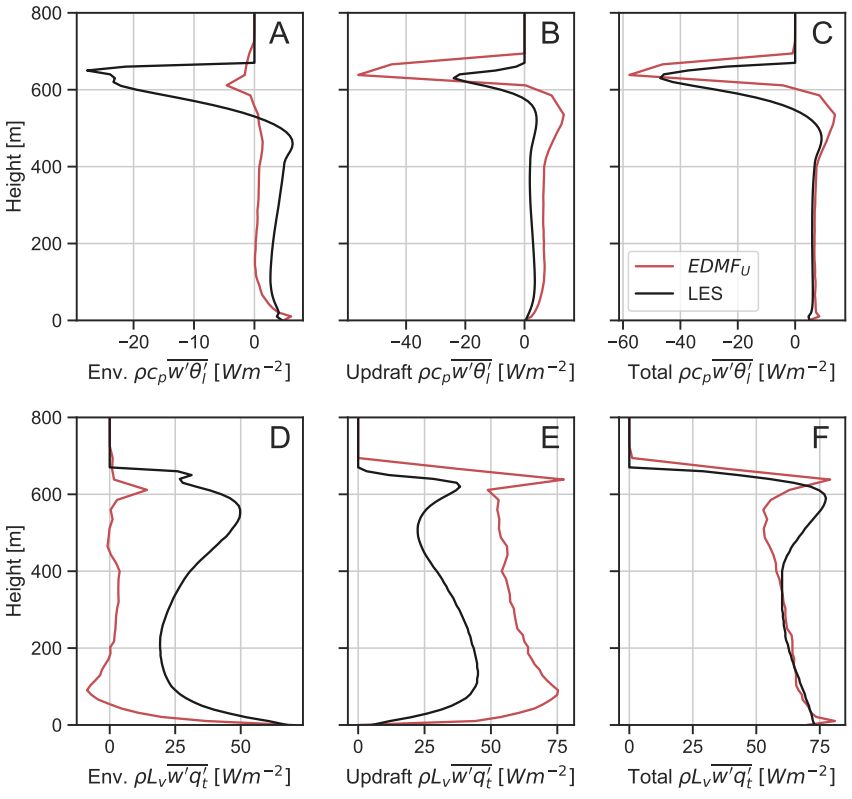

824 FIG. 11. CGILS case: WRF SCM heat and moisture flux contribution from eddy diffusivity (A and D), updraft
825 mass flux (B and E), and total flux (C and F).

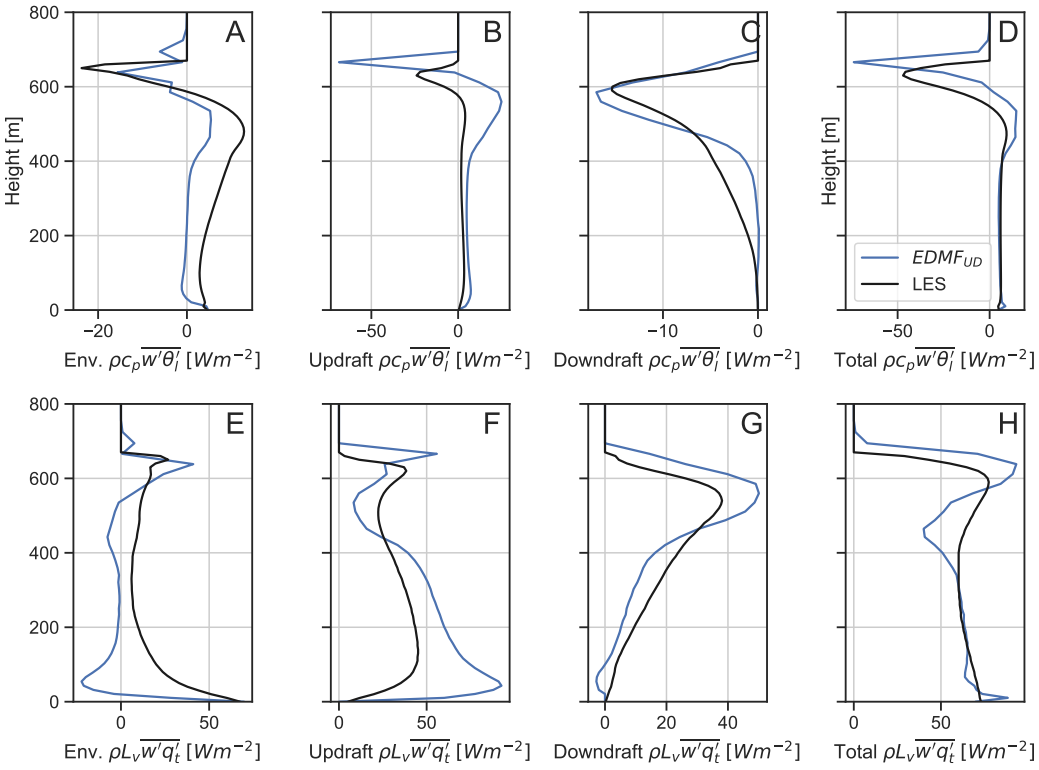

826 FIG. 12. CGILS case: WRF SCM heat and moisutre flux from individual component– eddy diffusivity (A and
827 E), updraft mass flux (B and F), downdraft mass flux (C and G), and total flux (D and H).

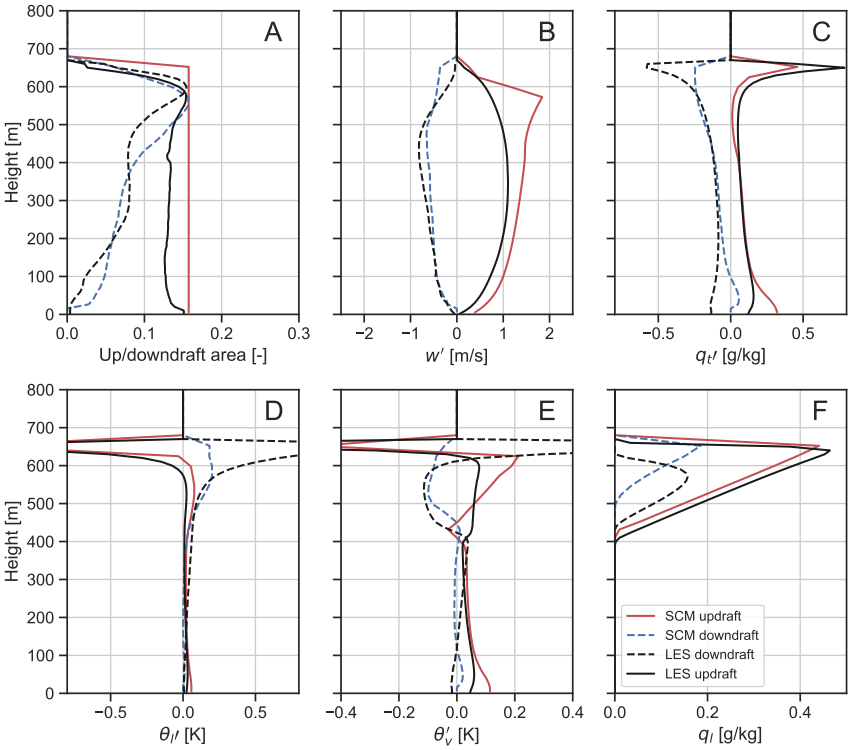

FIG. 13. CGILS case: WRF EDMF$_{UD}$ plume properties of (A) area, (B) vertical velocity perturbations, (C) total water mixing ratio perturbations, (D) liquid water potential temperature perturbations, (E) virtual potential temperature perturbations, and (F) liquid water content for both updraft (red solid) and downdraft (blue dashed). LES results as in Fig 3 are in solid dark (updraft) and dashed dark (downdraft) line.

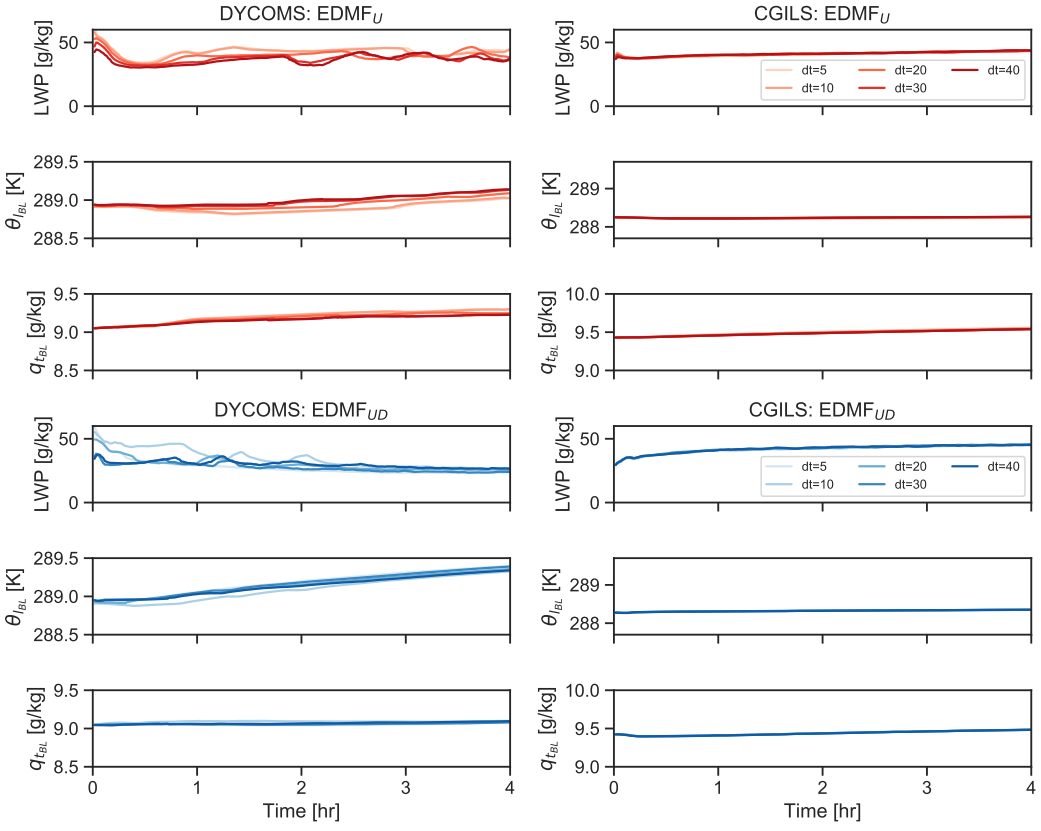

FIG. 14. Simulation results using different time step in EDMF$_U$ and EDMF$_{UD}$ for both DYCOMS and CGILS.